

Nanophotonic Enhancement and Improved Electron Extraction in Perovskite Solar Cells Using Near-Horizontally Aligned TiO₂ Nanorods

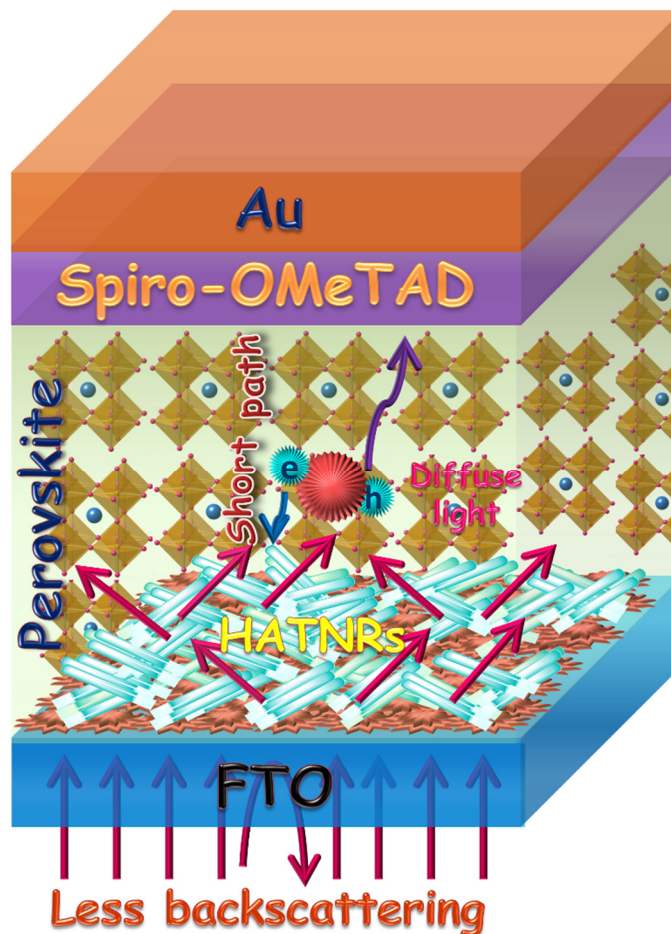
Ujwal K. Thakur¹, Sheng Zeng¹, Pawan Kumar¹, Sahil Patel¹, Ryan Kisslinger¹, Yun Zhang¹, Piyush Kar¹, Ankur Goswami¹, Thomas Thundat², Alkiviathes Meldrum³, and Karthik Shankar^{1*}

¹*Department of Electrical and Computer Engineering, University of Alberta, 9211-116 St, Edmonton, Alberta, T6G 1H9, Canada*

²*Department of Chemical and Materials Engineering, University of Alberta, 9211-116 St, Edmonton, Alberta, T6G 1H9, Canada*

³*Department of Physics, University of Alberta, Edmonton, Alberta T6G 2E1, Canada*

*Email: Karthik Shankar (kshankar@ualberta.ca)



Abstract

While vertically oriented metal oxide nanowires have been intensely researched for use as electron transport layers (ETLs) in halide perovskite solar cells (HPSCs), horizontal nanowires (oriented roughly parallel to the substrate) have received much less attention despite their higher photonic strength due to overlapping electric and magnetic dipolar Mie resonance modes. Herein, we demonstrate the fabrication of an assembly of horizontally aligned TiO₂ nanorods (HATNRs) on FTO substrates *via* a facile hydrothermal route. The HATNRs are employed as the ETL to achieve 15.03% power conversion efficiency (PCE) in HPSCs which is higher than the PCE of compact TiO₂ based devices (10.12%) by a factor of nearly 1.5. A mixed halide, mixed cation organometal perovskite FA_{0.83}MA_{0.17}Pb(Br_{0.17}I_{0.83})₃ with optimized composition is used as the active layer. The excellent refractive index matching between the perovskite and TiO₂, coupled with strong Mie scattering in the nanorod geometry results in broadband near-zero backscattering and high forward scattering, upon coating of HATNRs with perovskite. The maximum suppression of backscattering is found at ~ 600 nm. The HATNRs ETL also improves the extraction of electrons from the perovskite layer and results in superior blocking of carrier recombination at the perovskite layer/FTO interface.

Keywords: Photovoltaics, Solvothermal Growth, IMPS and IMVS, KPFM, Surface potential, Finite-difference time-domain simulation, Time-resolved photoluminescence.

1. Introduction

Sunlight is by far the most abundant renewable energy resource, and it will be necessary to harvest increasing amounts of sunlight to meet steadily growing global energy demand, estimated to reach 50 TW by 2050. The field of non-silicon non-chalcogenide photovoltaics has seen

astonishing improvements in performance through the use of halide perovskite semiconductors in the active layer. While photoconversion efficiencies (PCEs) of over 23% have been demonstrated, there remains further room for improvement in the open circuit voltages (V_{oc}) and short circuit current densities (J_{sc}) achievable [1-3]. To improve the efficiency of perovskite solar cells several possibilities are being investigated such as developing and doping electron/hole transporting materials, and incorporating quantum dots in perovskite absorbing layers [4-11]. However, not much effort has been devoted towards the management of photons in the solar cells for efficiency improvements. Atwater et al. reported that inefficiencies in the management of photons are the largest source of losses in J_{sc} and V_{oc} due to poor harvesting of photons near the semiconductor band-edge, non-radiative carrier recombination losses limiting the match of the solar cell to a black body radiator at the same temperature, poorly optimized angular distribution of emission due to radiative recombination of carriers, and changes in the entropy of photons [12]. The use of active layer light management through the use of nanophotonic architectures offers the largest potential to overcome these losses.

Strong forward scattering in the layer immediately preceding the halide perovskite absorber concomitant with suppressed backscattering is extremely useful in boosting solar cell efficiencies by allowing the use of thinner absorber layers. Multiple scattering slows down light propagation and increases the probability of photons being absorbed in the active layer. Thinner absorber layers that harvest the same amount of sunlight result in improved performance parameters (V_{oc} , J_{sc} , FF) due to shorter carrier extraction paths and reduced recombination. Thinner absorber layers are associated with lower non-radiative recombination losses, which in turn increases V_{oc} [13].

Keeping this in mind, we examined near-horizontal nano-raft geometries to improve the utilization of photons. There are a number of theoretical works (and some experimental ones as

well) showing that horizontal disc-shaped structures made of high refractive index materials can preferentially suppress backscattering by approaching the first Kerker condition [14-16]. While Kerker found that magnetic spheres suppressed backscattering, overlapping or interfering electric dipole and magnetic dipole modes in ellipsoidal or disc shaped high index materials such as GaAs and Si have been used to generate either a similar broadband suppression of the backscattering or a relative enhancement of the forward scattering [17-20]. Rutile phase TiO₂ has a lower refractive index (2.7) than GaAs (3.5) and Si (3.7) but is nevertheless high enough to show appreciable nanophotonic effects in the proper geometry.

One dimensional (1-D) nanostructures such as nanotubes and nanorods possess unique light trapping and charge transport properties [21-25]. Nanorods exhibit high electron mobility, long diffusion length, and better pore filling properties in comparison to compact and mesoporous TiO₂ films [26]. Most reports on the use of nanorods, have applied vertically oriented TiO₂ nanorod arrays as the electron transport layer in perovskite solar cells [27-30]. In comparison, there are almost no reports on horizontal or near-horizontal nanorods as the ETL in perovskite solar cells despite their superior photonic strength. Hydrothermal growth is the primary route for the synthesis of various TiO₂ nanostructures, wherein a TiO₂ precursor is hydrolyzed in the presence of water, heat and stabilizers. The hydrothermal method provides us the flexibility to engineer the architecture of the grown nanorods by changing the physical parameters such as growth time, temperature, precursor concentration, solvent, and the substrate positioning inside of the autoclave [27, 31].

2. Results and discussion

2.1 Growth of near-horizontally aligned TiO_2 nanorod ETLs

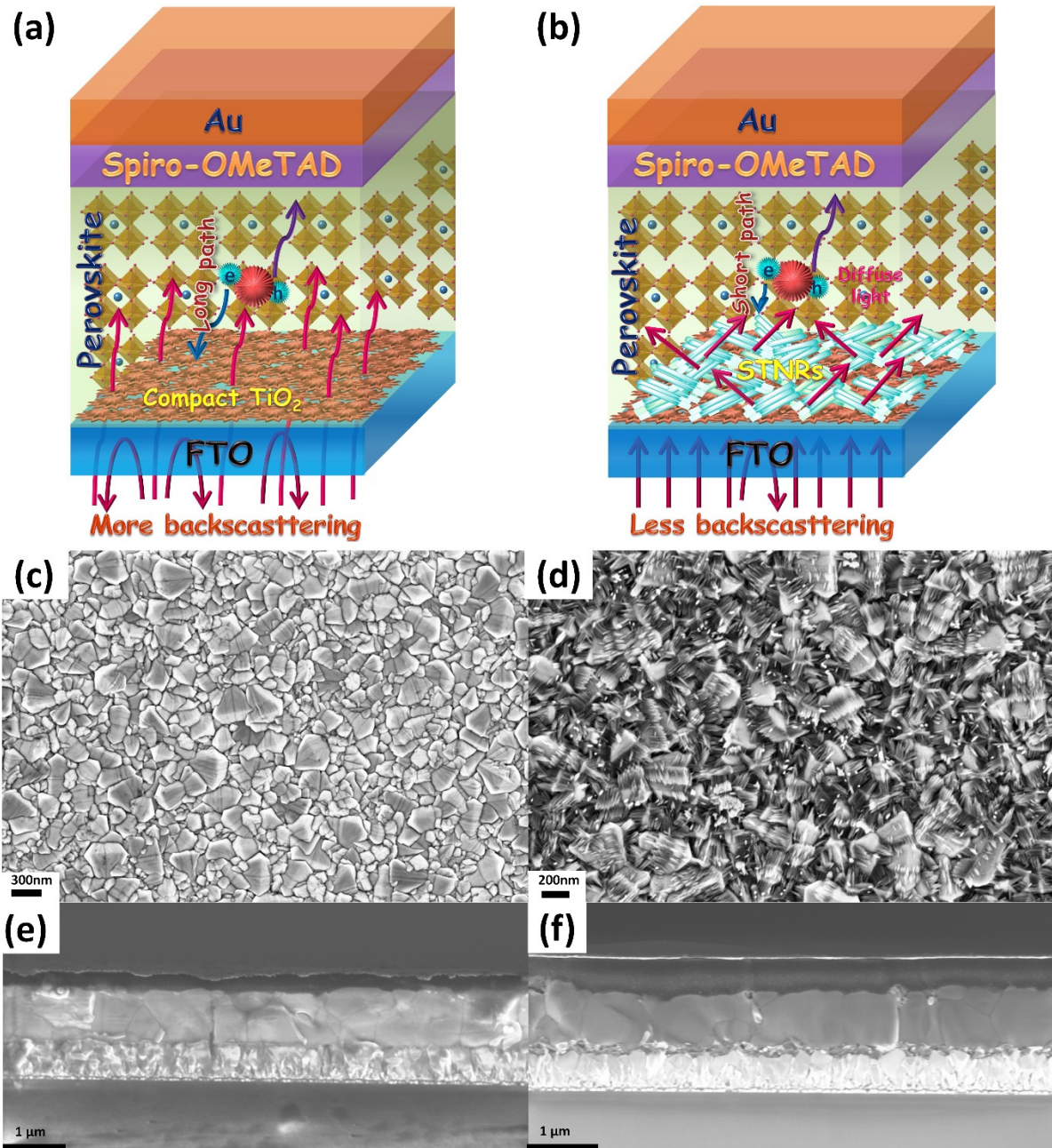


Fig. 1. Graphical representation of perovskite solar cells made with (a) Compact TiO_2 and (b) Nanostructured HATNRs obtained by hydrothermal method; Topographic FESEM image of (c) compact and (d) HATNRs. Cross-sectional view of a perovskite solar cell made with (e) Compact TiO_2 layer and (f) HATNR arrays.

Compact TiO₂ film on FTO glass substrate was obtained by spin coating precursor solution and annealing at 500°C while the HATNRs were grown on TiO₂ seed layers deposited on FTO glass *via* a facile hydrothermal reaction using titanium (IV) *n*-butoxide as TiO₂ precursor in the presence of hydrochloric acid (HCl), acetic acid (HAc) and water. Both films showed negligible parasitic absorption loss over the entire visible range (Fig. S1). Figs. 1a and 1b are schematic illustrations of *n-i-p* type perovskite solar cells made with compact TiO₂ and HATNR respectively. Figs. 1c and 1d are the top-view field emission scanning electron microscope (FESEM) images of the compact TiO₂ and HATNR respectively. In our previous report, we demonstrated the effect of the precursor concentration on the morphology of the resulting vertically oriented TiO₂ nanorods and its impact on the performance of perovskite solar cells based on them [25, 27]. In this non-organic recipe, we used titanium *n*-butoxide (TBO) as precursor and DI water as the primary solvent in which the nanorod growth reactions takes place. HCl and HAc both affect the morphology of the structure during growth. More specifically, the acids provide H⁺ ions which suppress the fast hydrolysis of TBO precursor, thereby leaving more precursor available for the growth of the nanorods. The growth of the crystal is mainly determined by the relative growth of the various crystal faces which bound a unit cell of the TiO₂ lattice. In rutile TiO₂, each Ti atom is bound to 6 oxygen atoms in an octahedral unit cell, and the growth of each face depends on the available coordination polyhedron. The crystal grows in the direction which minimizes surface energy, and thus is the most thermodynamically stable. The FTO substrate has a tetragonal rutile crystal structure, and the lattice mismatch between the tetragonal FTO ($a = b = 0.4687$ nm) and rutile TiO₂ ($a = b = 0.4594$) is only about 1.98% which promotes the nucleation and growth of the rutile phase TiO₂ nanostructures on the substrate [32-37]. Furthermore, the acids contribute Cl⁻ and CH₃COO⁻ ions which help in tuning the morphology of the crystalline nanostructures by retarding the growth

rate of the (110) plane. The size of the solvated ion affects the spacing between the individual nanorods grown. The morphology of the nanostructures is dependent on the recipe used during fabrication as well as on the substrate orientation. It is known that the effect of the angle at which the substrate is placed (with respect to the base of the Teflon reaction vessel) greatly affects the direction in which the nanorod arrays grow. This is true since the substrate orientation affects the precursor deposition which in turn affects the nucleation sites for further growth. We used these principles to tune the morphology of the TiO₂ nanostructures *via* the hydrothermal growth process such that near-horizontal bunches of nanorods (“nano-rafts”) formed instead of the typically observed vertical nanowire arrays.

The FESEM images (Figs. 1c and 1e) of compact TiO₂ deposited on FTO depicts an irregular film thickness with numerous discontinuous features or pin holes (see also Figs. S2a and S2d). The deposition of perovskite over this irregular and discontinuous TiO₂ layer results in a high probability of direct contact between bare FTO substrate and perovskite layer. The formation of this poor hole blocking layer promotes faster electron-hole recombination between the FTO and the perovskite layer which in turn reduces the charge transport efficacy of the ETL. The non-uniform compact TiO₂ layer, along with the presence of pinholes significantly reduces the performance of the device. These pinholes can be reduced by increasing the thickness of the compact TiO₂ film which would improve the hole blocking property of the film. However, the resulting thick and smooth compact TiO₂ surface increases the series resistance and reduces the interfacial area between the perovskite and ETL. This results in deterioration in the fill factor and the current density of the device. The FESEM images of titania nanorods grown on TiO₂ compact layer deposited FTO glass exhibit randomly distributed near-horizontally aligned nanorods bunched together as nanorafts (Fig. 1d). It can be seen in Figs. 1f, S2b and S2c that

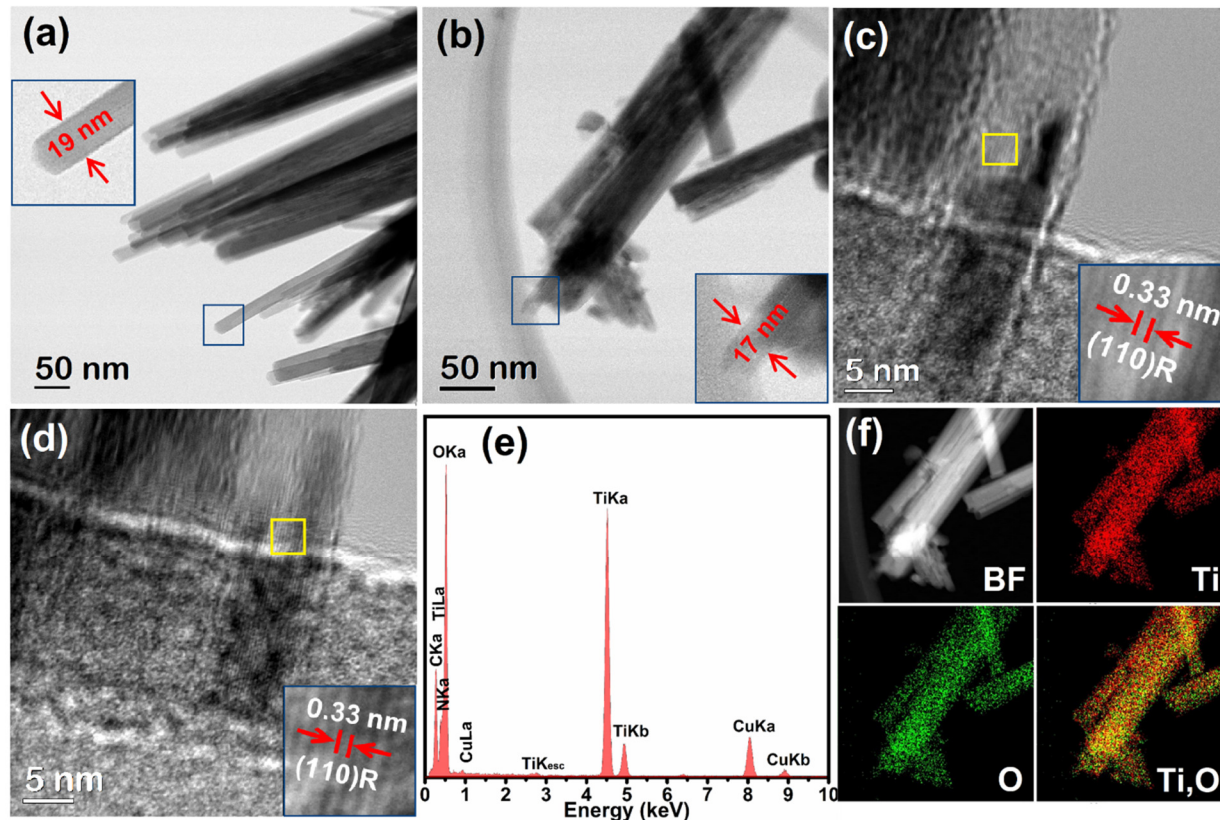


Fig. 2. (a, b) HR-TEM images HATNRs images at 50 nm scale bar showing bundles of nanorods and inset showing individual nanorods and their respective diameter (c, d) high magnification images at 5 nm scale bar showing lattice fringes (e) EDX pattern showing presence of Ti and O and (f) Bright field image and EDX elemental mapping for Ti, O and their summed-up image.

hydrothermally grown, TiO₂ nanorod film deposited over the FTO substrates provides better film uniformity, and well defined near-horizontally oriented nanorods. It is evident that the hydrothermal treatment promotes filling of the pinholes present in the compact TiO₂ layer and hence provides a superior hole blocking property. On the other hand, it also provides a highly irregular surface which significantly improves the mesoscopic effect, thus helping to improve the current density, and hence the PCE of the device.

Ultrafine morphological attributes of HATNRs were determined using high resolution transmission electron microscopy (HRTEM). TEM images of HATNRs at low magnification

shows cylindrical nanorods clumped together as bundle and average diameter of single nanorod was found to be *ca.* 17-19 nm (Fig. 2a and b). The high-resolution TEM images at higher magnification clearly show lattice fringes with 0.33 nm interplanar spacing corresponding to the (110) plane of rutile phase TiO₂. Further, EDX pattern clearly shows sharp peaks of Ti and O, and confirms the presence of TiO₂ (Fig. 2e). The peaks corresponding to C and Cu arise from carbon coated TEM grids. EDX elemental mapping in STEM mode shows an even distribution of Ti and O in nanorods and averaged images show homogeneous composition, which further confirms stoichiometric and highly crystalline TiO₂ nanorods (Fig. 2f).

The surface and sub-surface (up to ~ 10 nm) chemical composition of compact TiO₂ and HATNR was investigated using X-ray photoelectron microscopy (XPS) (Figs. 3a and 3b). XPS survey scan for elemental analysis of compact TiO₂ and HATNRs exhibited all the peaks relevant to Ti2p and O1s along with other low and high core level peaks (Ti3s, Ti3p, TiLLM, OKLL and O3s *etc*) (Fig. S3). Core-level high resolution XPS (HR-XPS) spectra of both compact TiO₂ and HATNRs show two symmetric peaks at binding energies of 458.57 and 464.22 eV assigned to Ti2p_{3/2} and Ti2p_{1/2} peak components of Ti⁴⁺ state in TiO₂ crystal lattice (Fig. 3a) [38, 39]. The positions of Ti2p_{3/2} and Ti2p_{1/2} peaks with a peak splitting of 5.76 eV verify O²⁻ coordinated Ti⁴⁺ in compact TiO₂ and HATNR [40, 41]. However, due to being constituted of the same compound, there were no visible changes in Ti2p peaks observed for anatase phase compact TiO₂ and rutile phase HATNRs. HR-XPS spectra of compact TiO₂ in O1s region can be deconvoluted into two peak components located at BE ≈ 529.78 and 531.34 eV. The peak component at BE value of 529.78 eV was attributed to crystal lattice oxygen bonded to Ti (Ti-O-Ti), while peak component centered at binding energy 531.34 eV originated from surface adsorbed -OH groups and non-lattice adventitious oxygens (Fig. 3b) [42]. The two O1s peak components for HATNRs were located

at BE \approx 529.74 and 531.11 eV corresponding to lattice bonded oxygens and surface adsorbed non-lattice adventitious oxygens. Very small shift (0.04 eV) in O1s components of HATNRs at 529.74 eV might be due to different chemical environment of oxygens in rutile TiO₂ (tetragonal geometry with slightly orthorhombic distortion of TiO₆ octahedron) and anatase state (tetragonal) in compact TiO₂ [43, 44].

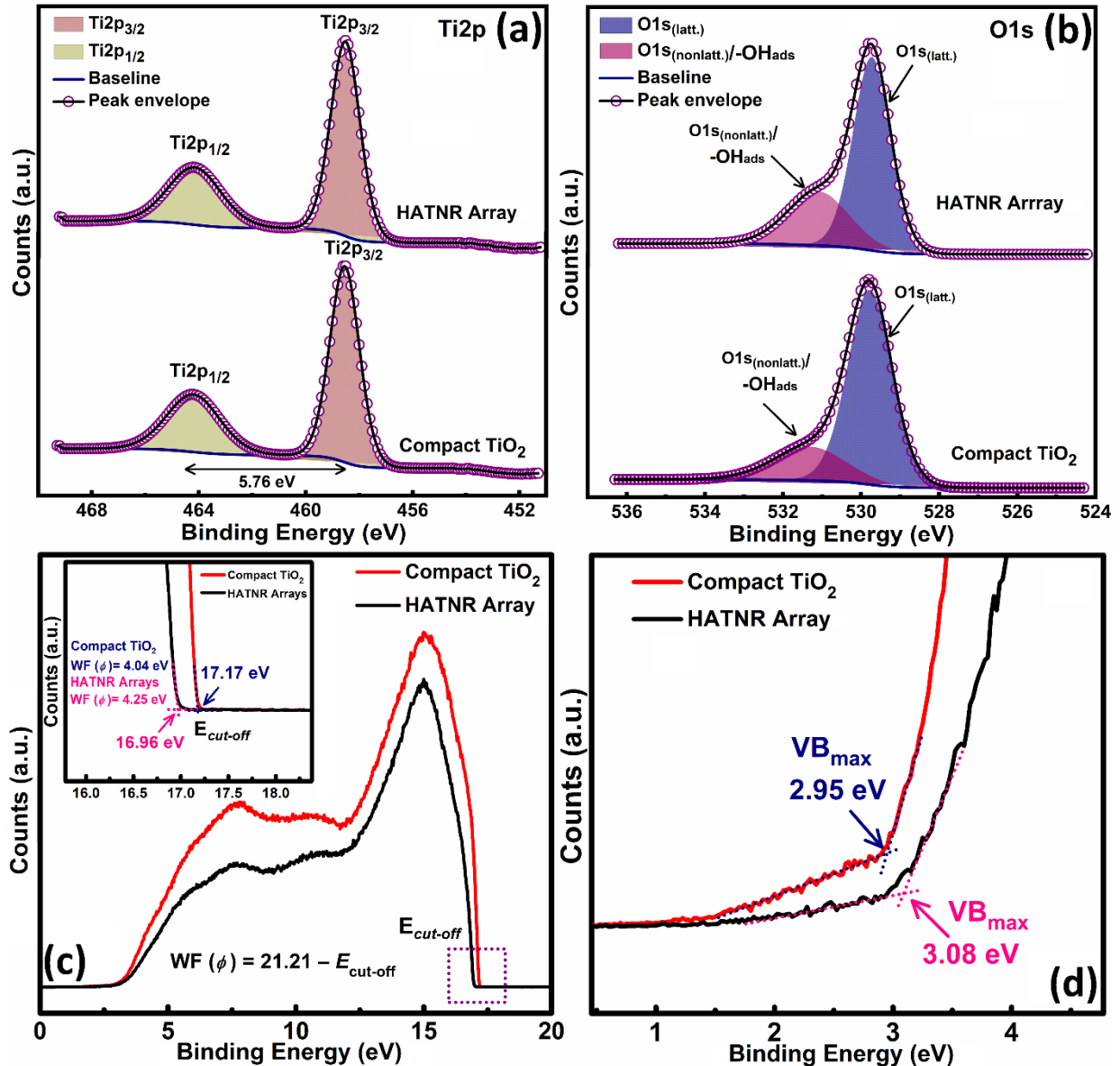


Fig. 3. HR XPS spectra of compact TiO₂ and HATNR array in (a) Ti2p region and (b) O1s region; (c) UPS work function spectra of compact TiO₂ and HATNR array. Inset shows the secondary electron cut-off energy ($E_{cut-off}$) while the value of work function (WF) was determined using the equation, $WF(\phi) = 21.21 - E_{cut-off}$,

where 21.21 eV is the energy of the incident He laser used for UPS (d) UPS valence band spectra showing position of valence band maxima (VB_{max}) below Fermi level.

To investigate the electronic band structure of the synthesized ETLs, work function and valence band spectra were measured using ultraviolet photoelectron spectroscopy (UPS) (Figs. 3c and 3d). The value of the work function (WF) was estimated from work function spectra using the expression $WF(\phi) = 21.21 - E_{cut-off}$, where 21.21 eV is the energy of the incident He laser light, and $E_{cut-off}$ is the cut-off energy of secondary electrons. The point of intersection by extrapolation of linear region of graph in horizontal and vertical regions gives the value of cut-off energy of secondary electrons ($E_{cut-off}$). The $E_{cut-off}$ values for compact TiO_2 and HATNR arrays were found to be 17.17 and 16.96 eV, and the corresponding work function values (ϕ) were calculated to be 4.04 and 4.25 eV, respectively (Fig. 3c and inset). Further, intersecting point of linear region in UPS valence band spectra gave the position of valence band maxima (VB_{max}). The VB_{max} values for the compact TiO_2 and HATNRs were calculated to be 2.95 and 3.08 eV below the Fermi level (Fig. 3d).

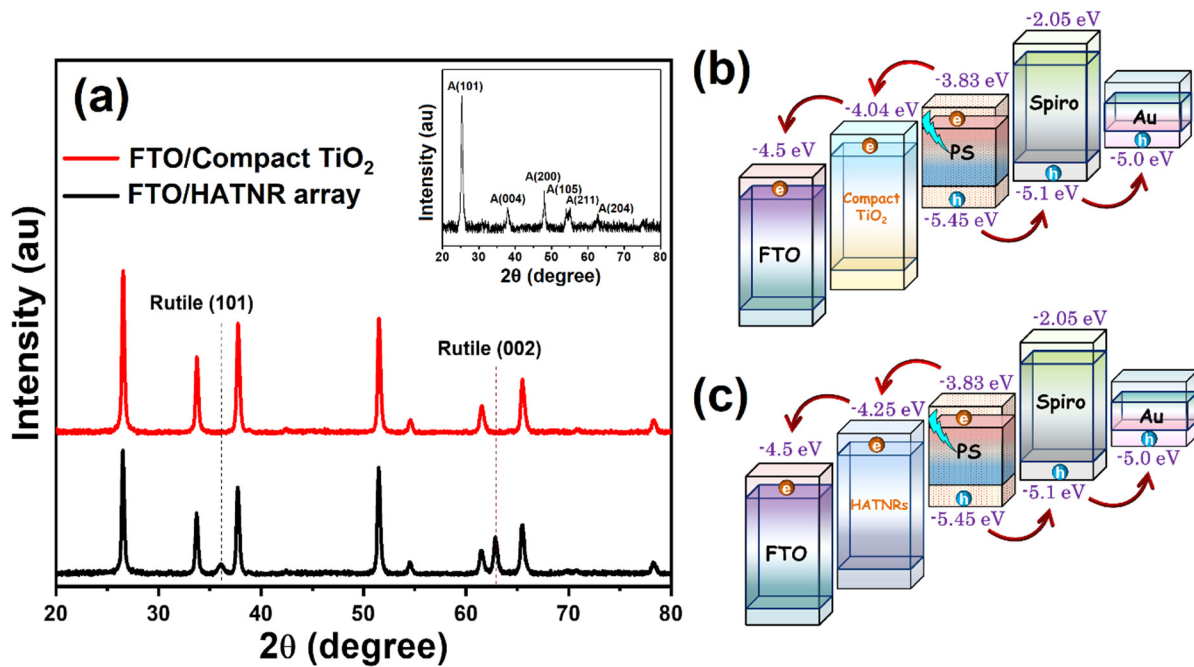


Fig. 4. (a) X-ray diffractograms of compact TiO₂ (red) and HATNR array (black) on FTO substrate. Inset shows XRD pattern of compact TiO₂ on bare glass substrate. Energy band diagram of perovskite solar cells made with (b) Compact TiO₂ and (c) HATNR arrays.

X-ray diffraction patterns of compact TiO₂ thin film and HATNR arrays were collected to investigate any change in crystallinity and phase structure (Fig. 4a). The XRD pattern of compact TiO₂ layer over FTO does not reveal any peak corresponding to the very thin compact TiO₂ layer due to the suppression of TiO₂ peaks by strong FTO diffraction peaks. However, the XRD pattern of blocking TiO₂ layer over bare glass substrate clearly reveals anatase peaks which match with JCPDS file no. 21-1272 and confirms the compact layer was composed of anatase TiO₂ (Inset of Fig. 2). For HATNR, two distinct rutile peaks at 2θ values of 62.82° and 36.09° were observed which was in excellent agreement with JCPDS file no. 21-1276 for tetragonal rutile phase TiO₂. HATNR array on compact TiO₂ can be considered as mixed phase TiO₂ because of the presence of underlying anatase compact TiO₂ and rutile nanorods. It is well documented in the literature that the conduction band of anatase phase TiO₂ is 0.2 eV higher than rutile phase TiO₂ in the absence of any heterojunction [45, 46]. This is also evident from UPS data where the difference between Fermi levels of anatase form in compact TiO₂ and rutile phase HATNRs was calculated to be 0.21 eV. Based on the UPS results we constructed the energy band diagram of solar cells made with compact TiO₂ and HATNR arrays and shown in Figs. 4b and 4c. While heterojunction formation anatase and rutile phase leads to type II (staggered) configuration. Fermi level alignment in mixed phase anatase-rutile heterojunction proceeds *via* charge redistribution and band bending which creates *n-n* heterojunction possessing higher conduction band position of rutile TiO₂ than anatase state. Scaloni *et al.* demonstrated that in heterojunction the conduction band of rutile phase TiO₂ was 0.4 eV higher than anatase form TiO₂ which facilitate facile transfer of electrons from the rutile to anatase TiO₂ [47]. Further, anatase TiO₂ possess low energy shallow traps 0.8 eV below

the conduction band of rutile so electrons can flow from rutile to anatase [47-49] which further helps in electron transfer resulting in significant improvement in the photovoltaic performance of HATNRs based solar cells. It is well known that the carrier transport efficiency of mixed phase TiO_2 is better compared to the pure anatase TiO_2 [50-54]. Furthermore, because of the presence of pinholes in the compact TiO_2 , perovskite can contact directly with the FTO electrode. Free electrons that have already been transferred to FTO can get reinjected into the valence band of perovskite because of a low interfacial energy barrier resulting in front surface recombination while in HATNR samples, the exposed FTO surface is passivated by rutile nanorods which results in elimination of direct contact between FTO and the perovskite layer.

2.2 ETL dependent carrier dynamics in halide perovskite solar cells

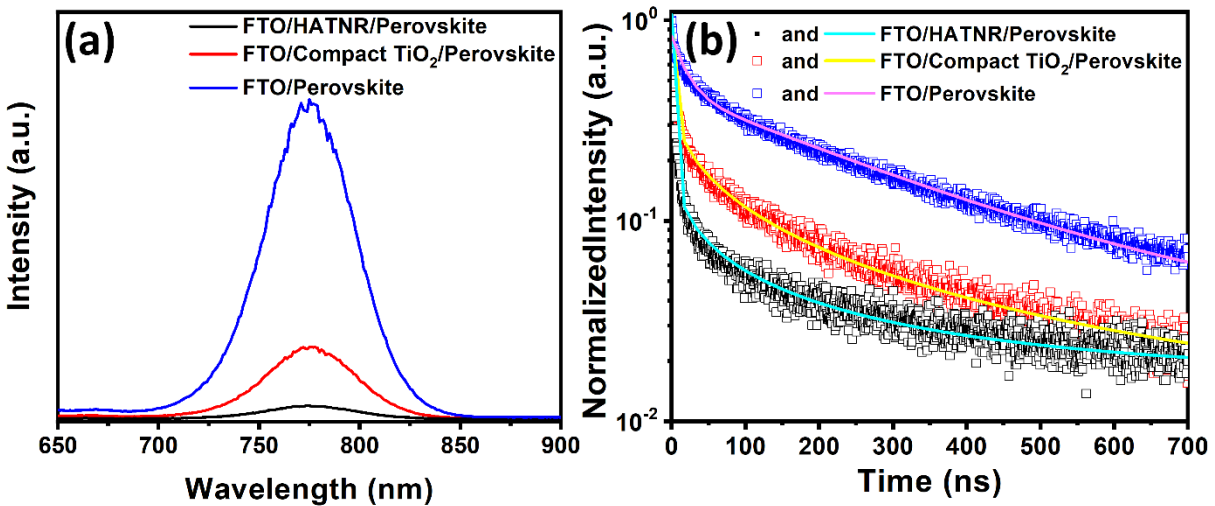


Fig. 5. (a) Steady state photoluminescence (PL) spectra of glass/perovskite (blue), perovskite deposited over compact TiO_2 (red) and perovskite/HATNR array (black); (b) The PL lifetime decay curve of perovskite with no ETL (blue; double exponential fit, magenta line), compact TiO_2 (red; double exponential fit, yellow line) and perovskite/HATNR array (black, double exponential fit, cyan).

To probe the carrier dynamics of these two different TiO_2 electron transporting layers, we compared the steady state photoluminescence (PL) spectra of perovskite on FTO glass with perovskite/compact TiO_2 /FTO glass and perovskite/HATNR arrays/FTO as shown in Fig. 5 (a).

The PL spectra of all samples exhibit an emission peak at 775 nm. The integrated PL intensity of perovskite on FTO glass was found to be highest, followed by perovskite/compact TiO₂/FTO glass, and perovskite/HATNR arrays/FTO samples respectively. Therefore, the HATNR array produced the greatest quenching of the perovskite luminescence. This observed PL quenching behavior was attributed to charge carrier extraction from the perovskite layer to the TiO₂ layers (ETLs). The higher PL quenching for nanostructured HATNR sample in comparison to the compact TiO₂ sample clearly indicates that the rate of electron transfer from the perovskite to the HATNR array assembly was faster than for compact TiO₂.

Time-resolved photoluminescence (TRPL) decay data were collected from the samples with compact TiO₂ and HTNR layers coated with perovskite, as well as from a perovskite sample without TiO₂ layers (Fig. 5b). The PL decay appears at least bi-exponential and the data were therefore fitted to the model:

$$I(t) = A_1 e^{-t/\tau_1} + A_2 e^{-t/\tau_2} \quad (1)$$

where A_1 and A_2 are scaling parameters, and τ_1 and τ_2 are the lifetimes of the shorter and longer decay components respectively. Both components are present almost equally in the perovskite layer, even in the absence of the ETLs, and the corresponding lifetimes τ_1 and τ_2 were 19.7 ns and 282.3 ns respectively, while the system response time is ~ 0.1 ns. For the ETL free samples, the decay is attributed mainly to trap-assisted recombination. The fast component is attributed to the bimolecular recombination of charge carriers trapped at the perovskite grain boundaries while the longer-lived component is most likely the radiative recombination of free electron-hole pairs. For the samples with ETL, the faster component is mainly related to the electron extraction from the perovskite layer to the electron transporting layer and the longer-lived component is attributed to the excited-state decay time or recombination dynamics of perovskite absorber [55-63]. For the

sample with the compact TiO₂ layer, the prefactor was slightly larger for the fast decay process while the corresponding lifetimes τ_1 and τ_2 were both significantly shorter (2.4 ns and 36.3 ns, respectively). For the HATNR based sample, the fast decay was dominant (the prefactor was almost 4 times larger) and the values of τ_1 and τ_2 were 2.9 ns and 23.4 ns, respectively. From these biexponential components, an average life time (τ_{ave}) can be obtained from a weighted mean by using eqn. (2) [64, 65].

$$\tau_{ave} = (A_1\tau_1^2 + A_2\tau_2^2) / (A_1\tau_1 + A_2\tau_2) \quad (2)$$

The average lifetimes of ETL-free, compact TiO₂ and HATNR samples were found to be 265.7 ns, 34.3 ns and 17.3 ns respectively. Thus, the HATNRs appear to create an especially fast non-radiative decay pathway, indicating that they effectively capture excited charge carriers in the perovskite layer. The shorter average lifetime of HATNRs relative to compact TiO₂ is consistent with a more effective electron transfer from the perovskite layer to the HATNRs, in agreement with the observed quenching of the steady-state PL.

Fig. S10 shows the topographical image of the perovskite layer deposited on top of the compact (Fig. S10a), and HATNR layers (Fig. S10b). Generally, the grain size of the polycrystalline perovskite layer depends on the deposition technique and the precursor used. However, we found that in spite of having an identical deposition technique and precursors, the average grain size of the perovskite deposited over the HATNR samples was larger than the average perovskite grain size deposited over the compact TiO₂ layer. The large grain size of perovskite over HATNRs can be explained by better entrapment of perovskite precursor solution in the voids between the HATNRs. As recombination (trap) centers in polycrystalline perovskite layer are generated by the grain boundaries, having a larger grain size helps to reduce undesirable non-radiative recombination and improve device performance [63, 66-69].

Kelvin Probe Force Microscopy (KPFM) is being intensively used to elucidate the nature of charge transport and recombination dynamics of charge transporting layers; we utilized it here to probe the transport properties of compact TiO₂ and HATNR [70-80]. Fig. S4 is the schematic illustration of KPFM measurement. Figs. 6a and 6b reveal the topography of halide perovskite layer deposited over compact TiO₂ film and HATNR arrays respectively. Figs. 6c and 6d represent the surface potential distribution on perovskite layer deposited over the compact TiO₂ and HATNR arrays in dark respectively. A key observation is that the surface potential is distributed evenly over the surface for perovskite coated on both the compact TiO₂ sample and the HATNR sample and is not influenced by the topographical variations seen in the AFM images. The KPFM measurement in dark (Figs. 6c and 6d) shows a contact potential difference (CPD) of -668 mV and -368 mV for compact TiO₂ and HATNR samples respectively. Thus, in the dark, the CPD (with respect to the FTO substrate) was strongly negative in both kinds of samples, which is attributed to downward bending of the electronic bands of perovskite at the perovskite-TiO₂ interface, a result that agreed well with previous reports [76, 77]. The surface potential of FTO/compact TiO₂/perovskite sample was more negative compared to FTO/HATNR/perovskite sample, indicating greater band-bending and redistribution of charge at the interface of the perovskite and compact TiO₂. The higher surface potential (less negative) in the dark in FTO/HATNR arrays/perovskite sample is indicative of a lower equilibrium electron density (N_D) in the HATNR arrays, in harmony with previously published reports on the low carrier concentrations obtained in hydrothermally synthesized TiO₂ nanorods [81, 82]. In a subsequent scan at the same position, the CPD recorded with continuous illumination using 450 nm laser was found to be shifted *ca.* +50 mV and +170 mV for compact TiO₂ and HATNRs (Figs. 6e and 6f) respectively due to effective charge separation, i.e. electrons moving to FTO through TiO₂ after

extraction from perovskite with hole remaining in the perovskite (Figs. 6d and 5e). The much higher surface potential of HATNR/perovskite samples provides direct evidence of superior charge separation and lower carrier recombination, which in turn, is indicative of lower surface defects and hence fewer electron traps compared to compact TiO₂/perovskite sample.

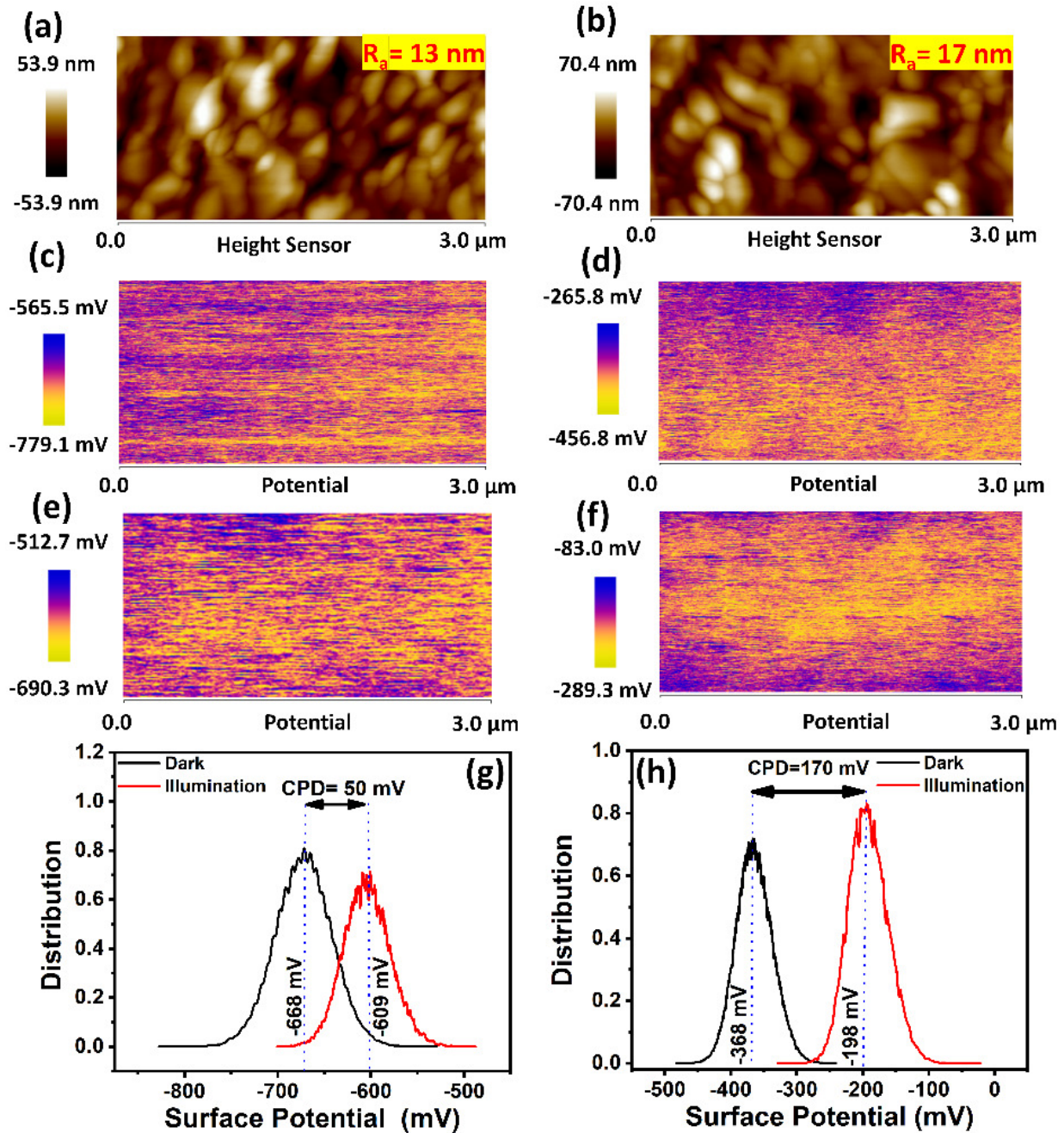


Fig. 6. Topography of perovskite layer deposited over compact TiO₂ (a) and HATNR (b). Surface potential map of perovskite deposited over compact TiO₂ (c) and HATNR (d) in dark. Surface potential map of perovskite deposited over compact TiO₂ (e) and HATNR (f) under illumination with 450 nm laser. Surface potential distribution on perovskite layer deposited over (g) compact TiO₂ and (h) HATNR in dark and under illumination with 450 nm laser.

The observed shift was found to be reversible after switching off the laser, which confirms that holes are accumulated on the surface of the perovskite while electrons transit through the ETL to the ground electrode (FTO substrate). Taken together, the surface potential data implies better charge separation and transport ability of HATNR ETL compared to compact TiO₂ ETL.

2.3 ETL dependent performance of halide perovskite solar cells

To probe the advantages of the near-horizontally aligned TiO₂ nanorods over the compact TiO₂, we fabricated perovskite solar cells with the procedure described in the methodology section (Section 1.3 in ESI). Fig. 7a depicts the *J-V* curves of perovskite solar cells fabricated with the compact TiO₂ and HATNR ETLs. The champion device employing the HATNRs exhibits a power conversion efficiency (PCE) of 15.03%, with a short circuit current density, open circuit voltage, and fill factor of 22.85 mA cm⁻², 0.99 V and 0.67 respectively. The champion device employing the compact TiO₂ layer exhibits a power conversion efficiency of 10.12% with a short circuit current density, open circuit voltage, and fill factor of 16.58 mA cm⁻², 0.99 V and 0.62 respectively.

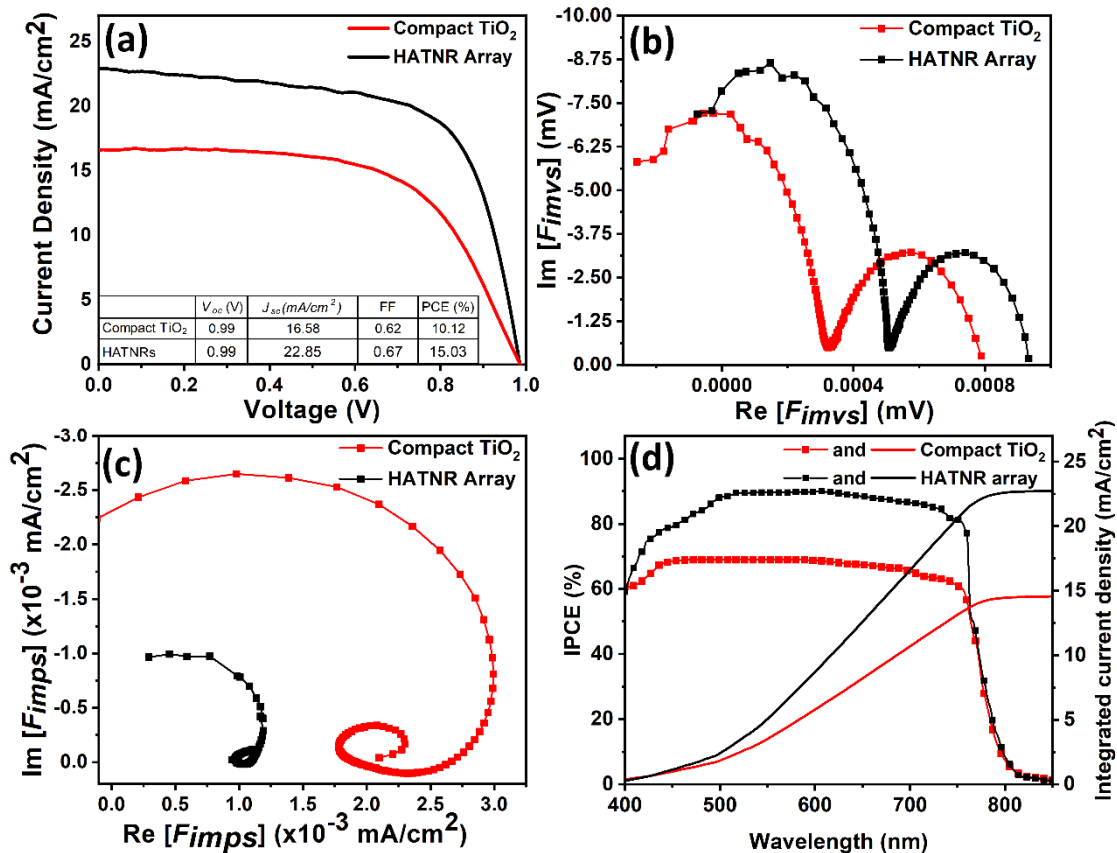


Fig. 7. Current density–voltage (*J-V*) curves measured under AM 1.5G condition (a), IMVS Nyquist plots measured with 633nm LED (b), IMPS Nyquist plots measured with 633nm LED (c) and external quantum yield of best-performing perovskite solar cells based on compact TiO₂ (red) and HATNR (black) electron transporting layers (d).

We further compared the performance of HATNR with vertically oriented TiO₂ nanorod arrays (VOTNRs). VOTNRs were fabricated using the same recipe used to fabricate HATNRs, except the FTO substrate was placed at an angle about 60° with respect to the bottom of autoclave. Cross-sectional and top view of resulting vertically oriented nanorods are shown in Figs. S5a and S5b respectively. Device made about 100 nm of vertically oriented TiO₂ nanorods gave a short circuit current density, open circuit voltage, and fill factor of 21.82 mA cm⁻², 0.96 V and 0.69 respectively which resulted in a PCE of 14.52% (Fig. S5c) which is comparable to our previous report [27].

The ETL composed of an assembly of HATNRs dramatically outperformed the compact TiO₂ and vertically oriented TiO₂ nanorod ETL and displayed 48.5% higher device efficiency compared to compact TiO₂ ETL. The performance of halide perovskite solar cells made with compact TiO₂ and HATNRs measured at AM 1.5G is summarized in Fig. S6 and Table S1. The improvement in the PCE was due to improvements in the short circuit current density and the fill factor which are related to the electron transfer and transport properties of ETL. To obtain additional insights into the electron transport and recombination dynamics in the photovoltaic devices with compact TiO₂ and HATNRs ETLs, small signal perturbation measurements, namely intensity modulated photovoltage spectroscopy (IMVS), and intensity modulated photocurrent spectroscopy (IMPS), were performed. Recently, these small perturbation techniques have been frequently used to study the charge carrier dynamics in perovskite solar cells [83-92]. Fig. 7b shows the IMVS response of a perovskite solar cell in the range of 0.1 Hz to 100 kHz. From the measurements, two semicircles - one in the high frequency region and another in the low frequency region were obtained with time constants τ_{hf} and τ_{lf} respectively. The obtained plot clearly shows two well resolved semicircles similar to the planar perovskite solar cells reported by Pockett *et al.* [93]. The recombination lifetimes of perovskite solar cells fabricated with HATNR and compact TiO₂ film were calculated by considering the frequency of the minimum point (f_{min}) of the high frequency semicircle, using eqn. (3).

$$\tau_r = 1/2\pi f_{min} \quad (3)$$

$$\tau_{et} = 1/2\pi f_{min} \quad (4)$$

The recombination time τ_r was calculated to be 3.14 μ s for HATNR and 3.20 μ s for compact TiO₂ solar cells. Similarly, the recombination lifetimes of HATNR and compact TiO₂ based solar cells in dark were calculated using solid state impedance spectroscopy shown (Fig. S7). As time

constants corresponding to carrier recombination for both types of electron transport layer are almost identical, no significant difference in the open circuit voltage is expected. To understand the charge transport properties of HATNR and compact TiO₂ films as ETLs, IMPS was used, and the resulting Nyquist plots are shown in Fig. 7c. The IMPS Nyquist plot of the perovskite solar cell has two distinct semicircles. One semicircle is in the first quadrant and the other is in the lower quadrant as reported in the literature for perovskite solar cells [93, 94]. Electron transport times (τ_{et}) within each ETL at short-circuit condition were calculated using eqn. (4), at the frequency corresponding to the minima of the imaginary photocurrent. τ_{et} was calculated to be 36.70 μ s for HATNR and 73.80 μ s for compact TiO₂ based solar cells. Lower transport time of HATNR indicated better charge transport efficiency of HATNRs which leads to improvement in the charge collection efficiency of the HATNR and hence the short-circuit current density.

$$D = d^2/2.35 \cdot \tau_{et} \quad (5)$$

$$L_D = (D \cdot \tau_r)^{1/2} \quad (6)$$

Charge transport rates within the ETL were calculated by estimating the electron diffusion coefficient, D , using eqn. (5), where the thicknesses (d) of the ETLs in the solar cells were considered. Values of D were found to be $46.70 \times 10^{-6} \text{ cm}^2 \text{ s}^{-1}$ for HATNR arrays and $28.25 \times 10^{-6} \text{ cm}^2 \text{ s}^{-1}$ for compact TiO₂ based solar cells, implying faster electron transport in HATNRs than in compact TiO₂. The corresponding carrier mobilities were estimated using the Einstein relation to be $1.80 \times 10^{-3} \text{ cm}^2 \text{ V}^{-1} \text{ s}^{-1}$ for the HATNR and $1.09 \times 10^{-3} \text{ cm}^2 \text{ V}^{-1} \text{ s}^{-1}$ for the compact TiO₂ ETL. Due to their high surface area, the nanorods are expected to have a large population of carrier traps that limit their mobility [82]. However, the diffusion coefficient (and electron mobility) of the HATNRs are more in line with surface passivated rutile TiO₂ nanorods [26, 81, 95], suggesting that the perovskite coating might be at least partially passivating the surface of the HATNRs.

Considering the values of D and τ_r , the effective electron diffusion length L_D was determined using eqn. (6) and were calculated to be 12.16 μm for the HATNR based solar cell and 10.61 μm for the compact TiO_2 based solar cell. The 15% higher electron diffusion length is expected to result in higher photocurrent densities and fill factors in HATNR array-based perovskite solar cells. The incident photon-to-electron conversion efficiency (IPCE) shown in Fig. 7d agreed well with the J_{sc} values obtained in the J - V curve. The IPCE values for the HATNR based perovskite solar cells were significantly larger than those for the compact TiO_2 based perovskite solar cells for the spectral range from 430 nm to 770 nm. The IPCE is given by product of the light harvesting efficiency (LHE), the charge separation efficiency (CSE) and the charge collection efficiency (CCE) as eqn. (7),

$$\text{IPCE (\%)} = \eta_{\text{LHE}} \times \eta_{\text{CSE}} \times \eta_{\text{CCE}} \quad (7)$$

The improved carrier extraction by the HATNR ETL demonstrated through stronger PL quenching and CPD shift in KPFM implies a higher charge separation efficiency while the higher electron diffusion lengths in the HATNR ETL inferred from IMPS data implies a higher charge collection efficiency resulting in higher IPCE and hence higher short-circuit current density of perovskite solar cells made with HATNR compared to the compact TiO_2 .

2.4 Nanophotonic enhancement of halide perovskite solar cells due to HATNR ETL

To understand the light harvesting properties (η_{LHE} in eqn. 7) of the compact, and HATNRs nanostructures, we performed UV-Vis measurements. The UV-Vis spectra of perovskite layer deposited TiO_2 structures are depicted in Fig. S9. The significantly lower diffuse reflectance of the perovskite coated HATNR ETL (black curve in Fig. S9a) compared to the perovskite coated compact TiO_2 ETL (red curve in Fig. S9a) for the same perovskite thickness demonstrates the

suppression of backscattering in the HATNR ETL-based solar cells. Likewise, the integrated absorptance of perovskite films on the HATNR ETL was found to be dramatically higher in comparison to the compact TiO₂ film in Fig. S9b over the entire visible range. The methodology of measurement of the integrated absorptance is explained in Section S1.4 and Fig. S8 in ESI. The strong forward light scattering by the HATNR slows down the propagation of light and also randomizes the direction of propagation, and both these effects enhance the absorption of photons within the perovskite active layer. When the morphology consists of one-dimensional nanostructures aligned horizontally on the substrate, they act as light scattering centers and facilitate the diffusion of photons, and hence increase the light absorption. Similar results have been reported by the Gao *et al.* when they used a TiO₂ nanotube network as the electron transport layer for perovskite solar cells [96].

Electromagnetic simulations were performed to validate our hypothesis regarding the nanophotonic enhancement effect using Lumerical FDTD Solutions. The compact layer was set up as 60 nm thick anatase TiO₂, while the individual nanorods were 20 nm in width and 100 nm in length. The HATNR ETL was composed of nanorods composed of square-shaped rutile TiO₂ nanorods tilted at 30 degrees lying on FTO glass. All the simulation parameters were based on FESEM images. Our hypothesis is that the HATNR nanostructure serves as a scatterer, which facilitates light diffusion and enhanced light absorption. To better understand light scattering effects and their relationship with the film morphology, far field scattering simulations were performed for both compact TiO₂ and HATNR ETLs with and without perovskite. Two different perovskite layer thicknesses were used 200 nm and 800 nm. The polar plots directly reveal the direction and intensity of scattering light. In the simulation, the light source is placed below the

sample and the sample is illuminated upwards along the z -direction. The substrate lies in the x - y plane. Forward-scattering is presented as the top semicircle from 0° to 180° while backscattering

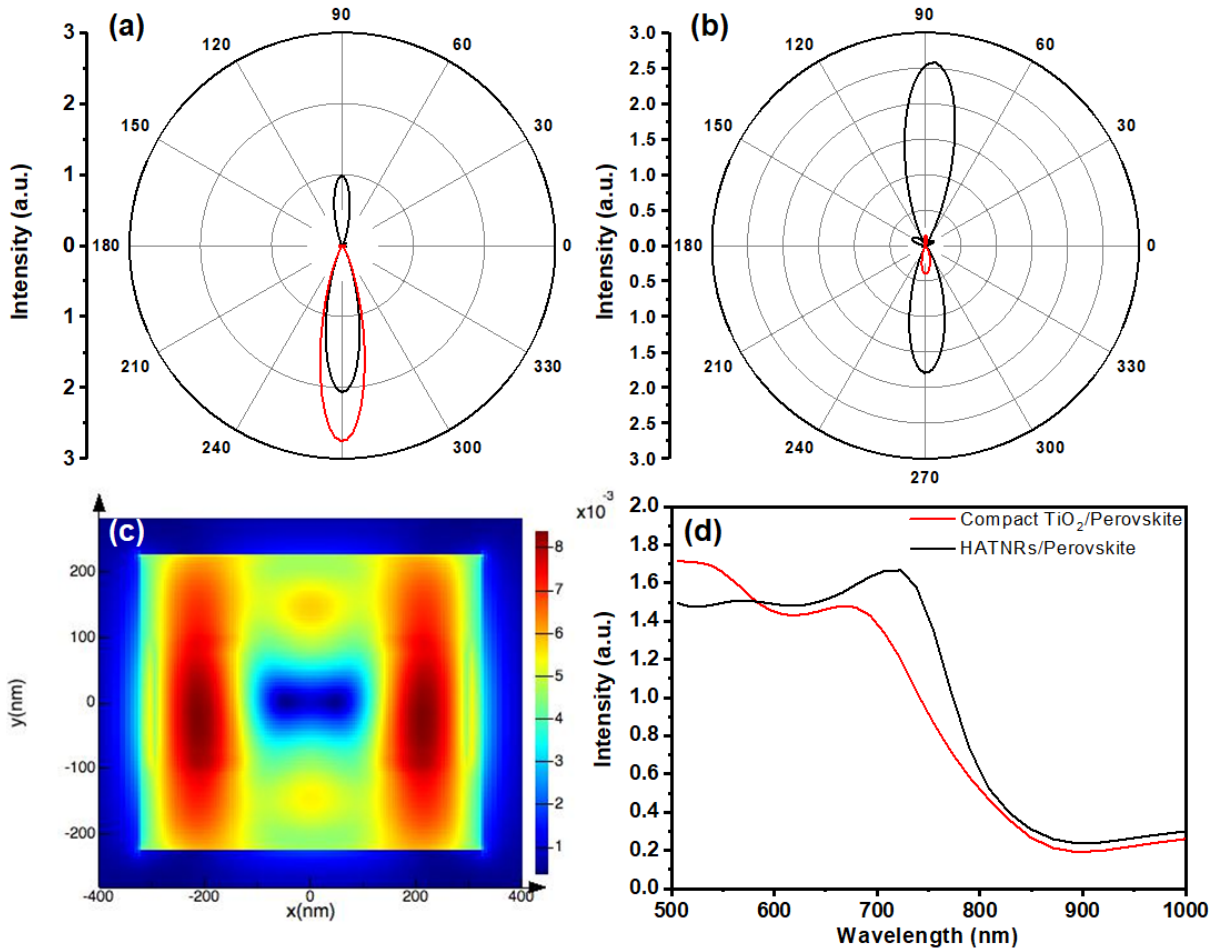


Fig. 8. Simulation data showing (a) scattering polar plot of compact TiO_2 ETL coated with perovskite thin films of 200 nm thickness (black curve) and 800 nm thickness (red curve) (b) scattering polar plot HATNR ETL coated with perovskite thin films of 200 nm thickness (black curve) and 800 nm thickness (red curve) (c) Electric field intensity in substrate plane for HATNR ETL immersed in perovskite matrix and (d) Absorption of compact TiO_2 (red) and TiO_2 nanorods (black) with 800 nm thick perovskite layer deposited on top.

is from 180° to 360° in both polar plots. Fig. 8a demonstrates that the compact TiO_2 ETL samples exhibit extremely strong backscattering, which is a major source of photon losses. For the compact

TiO₂ ETL, although the forward-scattering decreases after increasing the thickness of the perovskite layer, the backscattering is little changed as seen in Fig. 8a. Meanwhile, it is obvious from Fig. 8b that backscattering is well suppressed for the HATNR ETL, and the dramatic decrease of forward scattering intensity is attributed to enhanced absorption of diffused light by the perovskite layer on the top of the HATNR ETL. Fig. 8c is a simulated Poynting vector distribution in the x - y plane showing hotspots near the extremities of the major axis of the nanorods where maximum light absorption takes place. Fig. 8d consists of the simulated absorption spectra of two ETLs after coating with perovskite, and the enhanced light harvesting by the HATNR ETL based samples seen in the experimental data (Fig. 7d) is confirmed. These results fully validated our theory that high photonic strength of the near-horizontally aligned nanorods coupled with near-perfect refractive index matching with the perovskite layer, ensures maximum utilization of incident light within the perovskite layer. These results are applicable to other types of solar cells as well (such as those based on Si and GaAs). Nanorods consisting of non-absorbing or weakly absorbing horizontal nanorods aligned in the substrate plane will suppress backscattering and enhance forward scattering, provided that the refractive index of the nanorods is well-matched with the real part of the complex refractive index of the medium in which the nanorods are embedded (typically the active layer absorber). More information about the simulations is provided in the supporting information, such as architecture parameters, light source and monitors.

3. Conclusion

In summary, we demonstrated a facile approach to prepare near-horizontally aligned TiO₂ nanorod (HATNR) arrays *via* a hydrothermal route. Scanning electron microscopy showed the formation of larger grained perovskite films on the HATNR electron transport layer (ETL). Time-resolved photoluminescence measurements indicated that the HATNR extracted electrons more efficiently

from the perovskite layer compared to the commonly used compact TiO₂ electron transport layer while intensity modulated photocurrent spectroscopy suggested faster transport in the HATNR ETL. The HATNR ETL also resulted in a nanophotonic enhancement of the absorption in the perovskite active layer. Both experimentally measured and simulated optical spectra demonstrated a strong suppression of the backscattering in perovskite-coated nanorod layers relative to perovskite-coated compact TiO₂ layers, and a forward scattering-mediated enhancement of the light harvesting. As a consequence of the nanophotonic enhancement in the utilization of photons in the active layer as well as improved electron extraction and electron transport in perovskite solar cells employing HATNR ETLs, a dramatic enhancement of the overall solar cell performance was observed. Perovskite solar cells constructed using the HATNR ETL exhibited an average photoconversion efficiency (PCE) of $13.9 \pm 0.8\%$ and a champion device PCE of 15.0%, which is nearly 50% higher than perovskite solar cells constructed using the compact TiO₂ ETL, which exhibited an average photoconversion efficiency (PCE) of $9.4 \pm 0.8\%$ and a champion device PCE of 10.1%.

Conflict of Interest

There are no conflicts to declare.

Acknowledgements

The authors would like to thank the Natural Sciences and Engineering Research Council of Canada (NSERC), the National Research Council Canada (NRC), Future Energy Systems (FES) and CMC Microsystems for financial assistance. UKT would like to thank Alberta Innovates for graduate student scholarship funding. The University of Alberta Nanofab and National Research Council - National Institute for Nanotechnology (NRC-NINT) are acknowledged for providing access to characterization and fabrication facilities. Photovoltaic device fabrication and testing facilities

used equipment made available to Karthik Shankar through a Canada foundation for Innovation (CFI) grant, which was matched by the Alberta Small Equipment Grants Program (SEGP). Dr. Kai Kui, NRC-NINT is kindly acknowledged for HR-TEM analysis.

References

- [1] N.R.E.L. (NREL), in, <https://www.nrel.gov/pv/assets/pdfs/pv-efficiencies-07-17-2018.pdf>, 2018.
- [2] A. Polman, M. Knight, E.C. Garnett, B. Ehrler, W.C. Sinke, *Science*, 352 (2016) aad4424.
- [3] N.J. Jeon, H. Na, E.H. Jung, T.-Y. Yang, Y.G. Lee, G. Kim, H.-W. Shin, S. Il Seok, J. Lee, J. Seo, *Nature Energy*, 3 (2018) 682-689.
- [4] L. Etgar, P. Gao, P. Qin, M. Graetzel, M.K. Nazeeruddin, *Journal of Materials Chemistry A*, 2 (2014) 11586-11590.
- [5] C. Wang, Y. Li, C. Zhang, L. Shi, S. Tong, B. Guo, J. Zhang, J. He, Y. Gao, C. Su, J. Yang, *Journal of Power Sources*, 390 (2018) 134-141.
- [6] J.T.-W. Wang, J.M. Ball, E.M. Barea, A. Abate, J.A. Alexander-Webber, J. Huang, M. Saliba, I. Mora-Sero, J. Bisquert, H.J. Snaith, R.J. Nicholas, *Nano Letters*, 14 (2014) 724-730.
- [7] J. Dong, Y. Zhao, J. Shi, H. Wei, J. Xiao, X. Xu, J. Luo, J. Xu, D. Li, Y. Luo, Q. Meng, *Chemical Communications*, 50 (2014) 13381-13384.
- [8] K. Mahmood, B.S. Swain, H.S. Jung, *Nanoscale*, 6 (2014) 9127-9138.
- [9] J.H. Kim, P.-W. Liang, S.T. Williams, N. Cho, C.-C. Chueh, M.S. Glaz, D.S. Ginger, A.K.-Y. Jen, *Advanced Materials*, 27 (2015) 695-701.
- [10] J.W. Jung, C.-C. Chueh, A.K.-Y. Jen, *Advanced Materials*, 27 (2015) 7874-7880.
- [11] S.S. Shin, E.J. Yeom, W.S. Yang, S. Hur, M.G. Kim, J. Im, J. Seo, J.H. Noh, S.I. Seok, *Science* 356 (2017) 167-171.
- [12] A. Polman, H.A. Atwater, *Nat. Mater.*, 11 (2012) 174-177.
- [13] Y. Cui, D. van Dam, S.A. Mann, N.J.J. van Hoof, P.J. van Veldhoven, E.C. Garnett, E.P.A.M. Bakkers, J.E.M. Haverkort, *Nano Letters*, 16 (2016) 6467-6471.
- [14] R. Alaei, R. Filter, D. Lehr, F. Lederer, C. Rockstuhl, *Opt. Lett.*, 40 (2015) 2645-2648.
- [15] B.S. Luk'yanchuk, N.V. Voshchinnikov, R. Paniagua-Domínguez, A.I. Kuznetsov, *ACS Photonics*, 2 (2015) 993-999.
- [16] A.I. Kuznetsov, A.E. Miroshnichenko, M.L. Brongersma, Y.S. Kivshar, B. Luk'yanchuk, *Science*, 354 (2016) aag2472.
- [17] S. Person, M. Jain, Z. Lapin, J.J. Sáenz, G. Wicks, L. Novotny, *Nano Letters*, 13 (2013) 1806-1809.
- [18] Z. Wang, N. An, F. Shen, H. Zhou, Y. Sun, Z. Jiang, Y. Han, Y. Li, Z. Guo, *Nanoscale Research Letters*, 12 (2017) 58.
- [19] T. Shibanuma, P. Albella, S.A. Maier, *Nanoscale*, 8 (2016) 14184-14192.
- [20] M. Kerker, D.S. Wang, C.L. Giles, *J. Opt. Soc. Am.*, 73 (1983) 765-767.
- [21] I. Paramasivam, H. Jha, N. Liu, P. Schmuki, *Small*, 8 (2012) 3073-3103.
- [22] A. Mohammadpour, P. Kar, B.D. Wiltshire, A.M. Askar, K. Shankar, *Current Nanoscience*, 11 (2015) 593-614.
- [23] X. Liang, Y. Cheng, X. Xu, R. Dong, D. Li, Z. Zhou, R. Wei, G. Dong, S.-W. Tsang, J.C. Ho, *Applied Surface Science*, 451 (2018) 250-257.
- [24] Y. Zhu, Z. Song, H. Zhou, D. Wu, R. Lu, R. Wang, H. Wang, *Applied Surface Science*, 448 (2018) 23-29.
- [25] U.K. Thakur, R. Kisslinger, K. Shankar, *Nanomaterials*, 7 (2017) 95.

- [26] X. Feng, K. Zhu, A.J. Frank, C.A. Grimes, T.E. Mallouk, *Angewandte Chemie International Edition*, 51 (2012) 2727-2730.
- [27] U.K. Thakur, A.M. Askar, R. Kisslinger, B.D. Wiltshire, P. Kar, K. Shankar, *Nanotechnology*, 28 (2017) 274001.
- [28] X. Li, S.-M. Dai, P. Zhu, L.-L. Deng, S.-Y. Xie, Q. Cui, H. Chen, N. Wang, H. Lin, *ACS Applied Materials & Interfaces*, 8 (2016) 21358-21365.
- [29] C. Liu, R. Zhu, A. Ng, Z. Ren, S.H. Cheung, L. Du, S.K. So, J.A. Zapien, A.B. Djuricic, D. Lee Phillips, C. Surya, *Journal of Materials Chemistry A*, 5 (2017) 15970-15980.
- [30] S. Wu, C. Cheng, J. Jin, J. Wang, T. Peng, *Solar RRL*, 2 (2018) 1700164.
- [31] A. Kumar, A.R. Madaria, C. Zhou, *The Journal of Physical Chemistry C*, 114 (2010) 7787-7792.
- [32] W.-Q. Wu, B.-X. Lei, H.-S. Rao, Y.-F. Xu, Y.-F. Wang, C.-Y. Su, D.-B. Kuang, *Scientific Reports*, 3 (2013) 1352.
- [33] C.J. Howard, T.M. Sabine, F. Dickson, *Crystallographica Section B*, 47 (1991) 462-468.
- [34] P.A. Sedach, T.J. Gordon, S.Y. Sayed, T. Fürstenhaupt, R. Sui, T. Baumgartner, C.P. Berlinguette, *Journal of Materials Chemistry*, 20 (2010) 5063-5069.
- [35] B. Liu, E.S. Aydil, *Journal of the American Chemical Society*, 131 (2009) 3985-3990.
- [36] X. Wang, Y. Liu, X. Zhou, B. Li, H. Wang, W. Zhao, H. Huang, C. Liang, X. Yu, Z. Liu, H. Shen, *Journal of Materials Chemistry*, 22 (2012) 17531-17538.
- [37] M. Abd-Lefdil, R. Diaz, H. Bihri, M. Ait Aouaj, F.J.E.P.J.A.P. Rueda, *The European Physical Journal- Applied Physics*, 38 (2007) 217-219.
- [38] L. Zhu, M. Hong, G.W. Ho, *Nano Energy*, 11 (2015) 28-37.
- [39] J. Yan, H. Wu, H. Chen, Y. Zhang, F. Zhang, S.F. Liu, *Applied Catalysis B: Environmental*, 191 (2016) 130-137.
- [40] J. Park, T. Back, W.C. Mitchel, S.S. Kim, S. Elhamri, J. Boeckl, S.B. Fairchild, R. Naik, A.A. Voevodin, *Scientific Reports*, 5 (2015) 14374.
- [41] M. Tahir, N.S. Amin, *Applied Catalysis B: Environmental*, 162 (2015) 98-109.
- [42] J. Yan, G. Wu, N. Guan, L. Li, Z. Li, X. Cao, *Physical Chemistry Chemical Physics*, 15 (2013) 10978-10988.
- [43] C. Das, M. Richter, M. Tallarida, D. Schmeisser, *Journal of Physics D: Applied Physics*, 49 (2016) 275304.
- [44] Y. Izumi, *Coordination Chemistry Reviews*, 257 (2013) 171-186.
- [45] S.N. Habisreutinger, L. Schmidt-Mende, J.K. Stolarczyk, *Angewandte Chemie International Edition*, 52 (2013) 7372-7408.
- [46] L. Jing, S. Li, S. Song, L. Xue, H. Fu, *Solar Energy Materials and Solar Cells*, 92 (2008) 1030-1036.
- [47] D.O. Scanlon, C.W. Dunnill, J. Buckeridge, S.A. Shevlin, A.J. Logsdail, S.M. Woodley, C.R.A. Catlow, M.J. Powell, R.G. Palgrave, I.P. Parkin, G.W. Watson, T.W. Keal, P. Sherwood, A. Walsh, A.A. Sokol, *Nat. Mater.*, 12 (2013) 798.
- [48] D.C. Hurum, A.G. Agrios, K.A. Gray, T. Rajh, M.C. Thurnauer, *The Journal of Physical Chemistry B*, 107 (2003) 4545-4549.
- [49] D.C. Hurum, K.A. Gray, T. Rajh, M.C. Thurnauer, *The Journal of Physical Chemistry B*, 109 (2005) 977-980.
- [50] J. Liu, J. Huo, M. Zhang, X. Dong, *Thin Solid Films*, 623 (2017) 25-30.
- [51] P. Deák, B. Aradi, T. Frauenheim, *The Journal of Physical Chemistry C*, 115 (2011) 3443-3446.
- [52] W.-K. Wang, J.-J. Chen, X. Zhang, Y.-X. Huang, W.-W. Li, H.-Q. Yu, *Scientific Reports*, 6 (2016) 20491.
- [53] G. Li, C.P. Richter, R.L. Milot, L. Cai, C.A. Schmuttenmaer, R.H. Crabtree, G.W. Brudvig, V.S. Batista, *Dalton Transactions*, (2009) 10078-10085.
- [54] J. Ding, Y. Li, H. Hu, L. Bai, S. Zhang, N.J.N.R.L. Yuan, *Nanoscale research letters*, 8 (2013) 9.

- [55] Z. Zhu, J. Ma, Z. Wang, C. Mu, Z. Fan, L. Du, Y. Bai, L. Fan, H. Yan, D.L. Phillips, S. Yang, *Journal of the American Chemical Society*, 136 (2014) 3760-3763.
- [56] D. Bi, C. Yi, J. Luo, J.-D. Décoppet, F. Zhang, Shaik M. Zakeeruddin, X. Li, A. Hagfeldt, M. Grätzel, *Nature Energy*, 1 (2016) 16142.
- [57] L. Wang, C. McCleese, A. Kovalsky, Y. Zhao, C. Burda, *Journal of the American Chemical Society*, 136 (2014) 12205-12208.
- [58] G. Xing, N. Mathews, S. Sun, S.S. Lim, Y.M. Lam, M. Grätzel, S. Mhaisalkar, T.C. Sum, *Science*, 342 (2013) 344-347.
- [59] S.D. Stranks, G.E. Eperon, G. Grancini, C. Menelaou, M.J.P. Alcocer, T. Leijtens, L.M. Herz, A. Petrozza, H.J. Snaith, *Science*, 342 (2013) 341-344.
- [60] O. Gunawan, T.K. Todorov, D.B. Mitzi, *Applied Physics Letters*, 97 (2010) 233506.
- [61] J. Yin, J. Cao, X. He, S. Yuan, S. Sun, J. Li, N. Zheng, L. Lin, *Journal of Materials Chemistry A*, 3 (2015) 16860-16866.
- [62] L. Po-Wei, L. Chien-Yi, C. Chu-Chen, Z. Fan, W.S. T., X. Xu-Kai, L. Jiangjen, J.A. K.-Y., *Advanced Materials*, 26 (2014) 3748-3754.
- [63] Q. Chen, H. Zhou, T.-B. Song, S. Luo, Z. Hong, H.-S. Duan, L. Dou, Y. Liu, Y. Yang, *Nano letters*, 14 (2014) 4158-4163.
- [64] M. Shalom, S. Inal, C. Fettkenhauer, D. Neher, M. Antonietti, *Journal of the American Chemical Society*, 135 (2013) 7118-7121.
- [65] Y. Kang, Y. Yang, L.-C. Yin, X. Kang, L. Wang, G. Liu, H.-M. Cheng, *Advanced Materials*, 28 (2016) 6471-6477.
- [66] R.J. Stewart, C. Grieco, A.V. Larsen, J.J. Maier, J.B. Asbury, *The journal of physical chemistry letters*, 7 (2016) 1148-1153.
- [67] W. Nie, H. Tsai, R. Asadpour, J.-C. Blancon, A.J. Neukirch, G. Gupta, J.J. Crochet, M. Chhowalla, S. Tretiak, M.A. Alam, *Science*, 347 (2015) 522-525.
- [68] W.S. Yang, B.-W. Park, E.H. Jung, N.J. Jeon, Y.C. Kim, D.U. Lee, S.S. Shin, J. Seo, E.K. Kim, J.H. Noh, *Science*, 356 (2017) 1376-1379.
- [69] F. Huang, A.R. Pascoe, W.Q. Wu, Z. Ku, Y. Peng, J. Zhong, R.A. Caruso, Y.B. Cheng, *Advanced Materials*, 29 (2017).
- [70] R. Ranjan, A. Prakash, A. Singh, A. Singh, A. Garg, R.K. Gupta, *Journal of Materials Chemistry A*, 6 (2018) 1037-1047.
- [71] Y.J. S., S. Jan, K. Jincheol, S.A. Mahboubi, H. Shujuan, L. Jonathan, J.N. Joong, S.S. Il, G.M. A., H.-B. Anita, *Advanced Energy Materials*, 6 (2016) 1600330.
- [72] J.S. Yun, A. Ho-Baillie, S. Huang, S.H. Woo, Y. Heo, J. Seidel, F. Huang, Y.-B. Cheng, M.A. Green, *The Journal of Physical Chemistry Letters*, 6 (2015) 875-880.
- [73] K.Y. Chan, J.N. Joong, N.J. Hong, Y.W. Seok, S. Jangwon, Y.J. S., H.-B. Anita, H. Shujuan, G.M. A., S. Jan, A.T. Kyu, S.S. Il, *Advanced Energy Materials*, 6 (2016) 1502104.
- [74] N. Faraji, C. Qin, T. Matsushima, C. Adachi, J. Seidel, *The Journal of Physical Chemistry C*, 122 (2018) 4817-4821.
- [75] E. Edri, S. Kirmayer, A. Henning, S. Mukhopadhyay, K. Gartsman, Y. Rosenwaks, G. Hodes, D. Cahen, *Nano Letters*, 14 (2014) 1000-1004.
- [76] M. Salado, R.K. Kokal, L. Calio, S. Kazim, M. Deepa, S. Ahmad, *Physical Chemistry Chemical Physics*, 19 (2017) 22905-22914.
- [77] J.-J. Li, J.-Y. Ma, Q.-Q. Ge, J.-S. Hu, D. Wang, L.-J. Wan, *ACS Applied Materials & Interfaces*, 7 (2015) 28518-28523.
- [78] N. Adhikari, A. Dubey, D. Khatiwada, A.F. Mitul, Q. Wang, S. Venkatesan, A. Iefanova, J. Zai, X. Qian, M. Kumar, Q. Qiao, *ACS Applied Materials & Interfaces*, 7 (2015) 26445-26454.
- [79] L.K. Ono, Y. Qi, *The Journal of Physical Chemistry Letters*, 7 (2016) 4764-4794.

- [80] A. Dymshits, A. Henning, G. Segev, Y. Rosenwaks, L. Etgar, *Scientific Reports*, 5 (2015) 8704.
- [81] A. Mohammadpour, B.D. Wiltshire, Y. Zhang, S. Farsinezhad, A.M. Askar, R. Kisslinger, Y. Ren, P. Kar, K. Shankar, *Nanotechnology*, 28 (2017) 144001.
- [82] A. Mohammadpour, S. Farsinezhad, B.D. Wiltshire, K. Shankar, *physica status solidi (RRL) - Rapid Research Letters*, 8 (2014) 512-516.
- [83] A. Pockett, G.E. Eperon, N. Sakai, H.J. Snaith, L.M. Peter, P.J. Cameron, *Physical Chemistry Chemical Physics*, 19 (2017) 5959-5970.
- [84] J.H. Heo, H.J. Han, D. Kim, T.K. Ahn, S.H. Im, *Energy & Environmental Science*, 8 (2015) 1602-1608.
- [85] E. Guillén, F.J. Ramos, J.A. Anta, S. Ahmad, *The Journal of Physical Chemistry C*, 118 (2014) 22913-22922.
- [86] Y. Yang, K. Ri, A. Mei, L. Liu, M. Hu, T. Liu, X. Li, H. Han, *Journal of Materials Chemistry A*, 3 (2015) 9103-9107.
- [87] X. Zong, Z. Sun, H. Wang, J. Wang, M. Liang, S. Xue, *Chemical Communications*, 51 (2015) 14076-14079.
- [88] F. Giordano, A. Abate, J.P.C. Baena, M. Saliba, T. Matsui, S.H. Im, S.M. Zakeeruddin, M.K. Nazeeruddin, A. Hagfeldt, M. Graetzel, *Nature communications*, 7 (2016) 10379.
- [89] Y. Zhao, A.M. Nardes, K. Zhu, *Faraday discussions*, 176 (2015) 301-312.
- [90] Y. Zhao, A.M. Nardes, K. Zhu, *The journal of physical chemistry letters*, 5 (2014) 490-494.
- [91] Y. Zhao, K. Zhu, *The Journal of Physical Chemistry Letters*, 4 (2013) 2880-2884.
- [92] D. Bi, L. Yang, G. Boschloo, A. Hagfeldt, E.M. Johansson, *The journal of physical chemistry letters*, 4 (2013) 1532-1536.
- [93] A. Pockett, G.E. Eperon, T. Peltola, H.J. Snaith, A. Walker, L.M. Peter, P.J. Cameron, *The Journal of Physical Chemistry C*, 119 (2015) 3456-3465.
- [94] Q. Cui, X. Zhao, H. Lin, L. Yang, H. Chen, Y. Zhang, X. Li, *Nanoscale*, 9 (2017) 18897-18907.
- [95] X. Sheng, L.P. Chen, T. Xu, K. Zhu, X.J. Feng, *Chemical Science*, 7 (2016) 1910-1913.
- [96] X. Gao, J. Li, S. Gollon, M. Qiu, D. Guan, X. Guo, J. Chen, C. Yuan, *Physical Chemistry Chemical Physics*, 19 (2017) 4956-4961.

SUPPORTING INFORMATION

Nanophotonic Enhancement and Improved Electron Extraction in Perovskite Solar Cells Using Near-Horizontally Aligned TiO₂ Nanorods

Ujwal K. Thakur¹, Sheng Zeng¹, Pawan Kumar¹, Sahil Patel¹, Ryan Kisslinger¹, Yun Zhang¹, Piyush Kar¹, Ankur Goswami¹, Thomas Thundat², Alkiviathes Meldrum³, and Karthik Shankar^{1*}

¹*Department of Electrical and Computer Engineering, University of Alberta, 9211-116 St, Edmonton, Alberta, T6G 1H9, Canada*

²*Department of Chemical and Materials Engineering, University of Alberta, 9211-116 St, Edmonton, Alberta, T6G 1H9, Canada*

³*Department of Physics, University of Alberta, Edmonton, Alberta T6G 2E1, Canada*

*Email: Karthik Shankar (kshankar@ualberta.ca)

S1. Materials and Methods

S1.1 Materials

Titanium (IV) *n*-butoxide (99%), titanium (IV) isopropoxide (98+%), acetonitrile (99.8%), lead iodide (99%) and lead bromide (98+%) were purchased from Acros Organics. Acetic acid (99.8%), HCl (37%), Formamidinium iodide ($\geq 98\%$), 4-*tert*-butylpyridine (96%), lithium bis(trifluoromethanesulfonyl)-imide (99.95%) and spiro-OMeTAD (99%) were procured from Sigma-Aldrich. Methylammonium bromide (98%) was obtained from Dyesol. Chlorobenzene (99+%), titanium (IV) chloride (99.9%), dimethylformamide (DMF) ($\geq 99.8\%$) and dimethylsulfoxide (DMSO) ($\geq 99.9\%$) were purchased from Fisher Scientific. The obtained chemicals were used as received without any further purification. All other chemicals were of

HPLC grade. Fluorine-doped tin oxide (FTO) coated glass slides purchased from Hartford Tec Glass Company were cleaned by ultrasonication in acetone, methanol and deionized water respectively for 10 minutes each. Cleaned substrates were dried using a nitrogen gun. About 60 nm of compact TiO₂ seed layer was then deposited onto the cleaned FTO: glass substrates. The precursor solution for the deposition of compact TiO₂ was prepared by a method described in our previous report [27].

S1.2 Synthesis of horizontally aligned TiO₂ nanorod (HATNR) arrays

Horizontally aligned TiO₂ nanorod (TNR) arrays were grown on FTO substrates seeded with TiO₂ compact layer by a simple hydrothermal approach. In brief, 85 μL of titanium (IV) *n*-butoxide was added to a 10 mL solution of HCl/HAc/DI water in a volume ratio of 1:1:2. The obtained mixture was transferred into a teflon-lined stainless-steel autoclave. The FTO substrate having TiO₂ seed layer was oriented vertically inside the autoclave by maintaining an angle of 90° to the bottom of the autoclave. The autoclave was then sealed and put in oven at 190°C for 60 min to achieve hydrothermal growth of nanorods. After completion of reaction, the autoclave was cooled to room temperature under ambient air and resultant transparent nanorod array on FTO substrate was rinsed with DI water for 2 min and dried in a stream of flowing nitrogen. To completely cover any exposed with TiO₂, a thin layer of TiO₂ was deposited by treating HATNR arrays with 40 mM of TiCl₄ at 70°C for 60 min and annealed at 500°C for 30 min.

S1.3 Device fabrication

The perovskite precursor solution was made by dissolving 1 M of formamidinium iodide (FAI), 1.1 M PbI₂, 0.2 M methylammonium bromide (MABr) and 0.22 M PbBr₂ in a 4:1 mixture of DMF:DMSO respectively. The obtained precursor solution was then stirred at 70°C for 2 h followed by deposition on top of the TNRs. The perovskite solution was deposited on TNRs in a two-step procedure: firstly at 1000 rpm for 10 seconds, and secondly at 4000 rpm for 20 seconds respectively. Further, 100 μL of chlorobenzene was dropped on the spinning substrate after 15 second after second step for rapid crystallization. The substrates were then annealed at 100°C for 30 min. After that, approx. 300 nm thick hole transporting layer was deposited by spin-casting the solution containing 72 mg Spiro-MeOTAD, 17.5 μL of stock solution of 520 mg mL⁻¹ bis(trifluoromethanesulfonyl)-imide in acetonitrile and 28.8 μL of 4-*tert*-butylpyridine in 1 mL of chlorobenzene. Finally, about 70 nm of gold was evaporated using e-beam evaporator to complete the device.

S1.4 Characterization

The morphological characteristics of the TiO₂ layers on FTO and fabricated perovskite solar cells were elaborated by using field emission scanning electron microscopy (FE-SEM) on Zeiss Sigma FESEM with an accelerating voltage 3 kV equipped with GEMINI in-lens detector. Fig. S1 shows cross-sectional images of the compact TiO₂ ETL and HATNR ETL. The UV-Vis-NIR absorption spectroscopy was performed using a Perkin Elmer Lambda-1050 spectrophotometer equipped with a 100 mm integrating sphere accessory in configuration(s) illustrated in Fig. S2. When a transmission measurement was performed without the use of the integrating sphere, photons scattered out of the sample in the forward direction are not captured by the photodetector due to which the sample extinction is overestimated. When the sample is placed at the entrance of the integrating sphere, corresponding to position (a) in Fig. S8, photons scattered out of the sample in the forward direction are reflected off the walls of the integrating sphere and registered by the photodetector, thus providing a more accurate estimate of the overall extinction. When the sample is placed the exit of the integrating sphere, corresponding to position (c) in Fig. S8 without a spectralon chuck behind the sample, a direct measurement of the diffuse reflectance i.e. backscattered intensity, is obtained. When the sample is placed in the middle of the integrating sphere, corresponding to position (b) in Fig. S8 with port (c) closed, both the transmitted and reflected photons remain in the sphere and are captured by the photodetector. However, one problem with this configuration is that photons bouncing off the walls of the sphere might perform multiple passes through the sample, thus causing the absorptance of the samples to be overestimated. When the sample is placed the exit of the integrating sphere, corresponding to position (c) in Fig. S8 but with a spectralon chuck behind the sample, no light is transmitted; previously transmitted photons are reflected off the spectralon chuck and make a second pass through the sample such that the only photons leaving the sample to be recorded by the photodetector are photons not absorbed by the sample. Thus, a direct measurement of the sample absorptance is rendered possible. This configuration also provides the closest approximation to the real situation in a photovoltaic device since the vacuum deposited metallic top electrode contact reflects photons back into the active layer similar to the spectralon chuck.

Steady state photoluminescence (PL) spectra were collected using a Varian Cary Eclipse Spectrofluorometer. Time-resolved photoluminescence (TRPL) curves were recorded using a homemade single photon counting setup. Samples were photoexcited by 405-nm picosecond diode

laser (Alphas GmbH) operated at a frequency of 1 MHz to excite the samples, and a Becker-Hickl HPM-100-50 PMT interfaced to an SPC-130 pulse counter system. This setup has a response time of ~ 100 ps. Intensity-modulated photovoltage spectroscopy (IMVS) and intensity-modulated photocurrent spectroscopy (IMPS) measurements were carried out on a Zahner Zennium electrochemical workstation (Zahner, Zennium) with a frequency response analyzer under a modulated 629 nm light emitting diode driven by a Zahner, PP211 source supply. The modulated light intensity was less than 10% base light intensity. The frequency range was set from 100 kHz to 0.1 Hz. The current-voltage characteristics of the samples were measured using a Keithley 4200 semiconductor parameter analyzer. For solar cell testing, one sun AM 1.5 G illumination from a collimated Class A solar simulator (Newport Instruments) was used. The incident photon-to-electron conversion efficiency (IPCE), also known as the external quantum efficiency (EQE) was calculated using a home-built set-up consisting of a Xe arc lamp, a chopper, a filter-wheel, a computer-controlled monochromator, a calibrated silicon photodetector, and an optical power meter.

The fine morphological features of material were determined using High resolution transmission microscopy (HR-TEM) EDX spectra and elemental mapping. The low-resolution TEM images and EDX spectral mapping was performed on a JEOL JEM-ARM200CF S/TEM equipped with STEM EDX detector, operating at an acceleration voltage of 200 keV. While High resolution TEM images was recorded on a JEOL 2200 FS TEM/STEM equipped with STEM EDX detector, operating at an acceleration voltage of 200 keV. The sample for low magnification images was prepared by scratching the samples using razor and sonicating in methanol to separate nanorods from the substrate followed by deposition on a lacy carbon coated copper TEM grid. While for high magnification images scratched sample was deposited directly on lacy carbon coated TEM grid. The acquired electronic images in .dm3 format was processed using Gatan micrograph to determine size of nanorods and interplanar d spacing. Elemental mapping files were processed with INCA Energy software.

To determine the surface chemical composition and oxidation state of materials Binding energy of compact TiO₂ and HANTR arrays were determine using XPS measurement acquired on a XPS (Axis-Ultra, Kratos Analytical) instrument equipped with monochromatic Al-K α source (15 kV, 50 W) and photon energy of 1486.7 eV under ultrahigh vacuum ($\sim 10^{-8}$ Torr). Exact binding energies were determined from the position of the adventitious C 1s peak at ≈ 284.8 eV and peaks

of other elements was assigned with respect to C1s peak. The deconvolution of raw data was done by using CasaXPS and extracted .csv files were later plotted in origin 8.5. Work function spectra and valence band spectra of materials were acquired by ultraviolet photoemission spectroscopy (UPS) performed with a 21.21 eV He lamp source. Peak force KPFM was performed on ETL and STNL samples using Dimension Fast Scan Atomic Force microscope ((Bruker Nanoscience Division, Santa Barbara, CA, USA) in presence and absence of diode laser (Thorlabs) of 450 nm wavelength. The laser was shined perpendicularly from of the sample through a custom-made optical setup. Pt coated SiN cantilever of 2.5 N/m stiffness was employed to conduct the KPFM experiments. The surface potential of the samples was measured at 100 nm lift height at 1 kHz lockin bandwidth. The scan speed was maintained 0.5 Hz. Both the samples were grounded with the AFM chuck with a conducting copper tape. The surface potential was mapped by sample routing at zero tip bias. Before doing the dark and illuminated conditions were maintained for 5 min before performing the experiments in order to obtain the equilibrium condition of carrier transport. Work function of Pt-Ir tip was calibrated by measuring the contact potential difference (CPD) of HOPG and the Pt tip using the following equation and found to be 5.04 eV.

$$E_{F(\text{tip})} = 4.6 \text{ eV (Work function of HOPG)} + V_{\text{CPD}}(\text{HOPG and Pt tip})$$

S1.5 Simulations

Simulations were performed using Lumerical FDTD Solutions. All the morphological parameters are based on FESEM images. In each case, the compact TiO₂ and HATNR ETLs were immersed in a MAPbI₃ perovskite layer of the relevant thickness. The compact anatase layer was set to be 100 nm thick. The nanorods constituting the HATNR ETL were 600 nm in width, 200 nm in length and 60 nm in thickness, which is a cuboid whose long edge is inclined at an angle of 30 degrees to the underlying FTO glass substrate. A TFSF (time-field scattered-field) light source, wavelength starting from 300 nm to 1000 nm produced a plane wave that propagated upward with a wave-vector normal to FTO surface. A far-field *close box* was set to monitor the scattered light power. An *Abs* monitor was applied to analyze the spatial and total absorption profiles. Several frequency-domain field and power monitors were employed to obtain information regarding the reflection, transmission, electric field and Poynting vector.

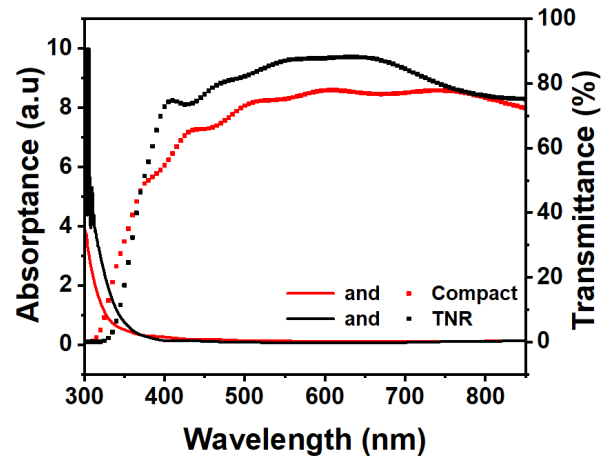


Fig. S1. Absorbance and transmittance spectra of compact TiO_2 and HATNR array deposited over FTO substrate.

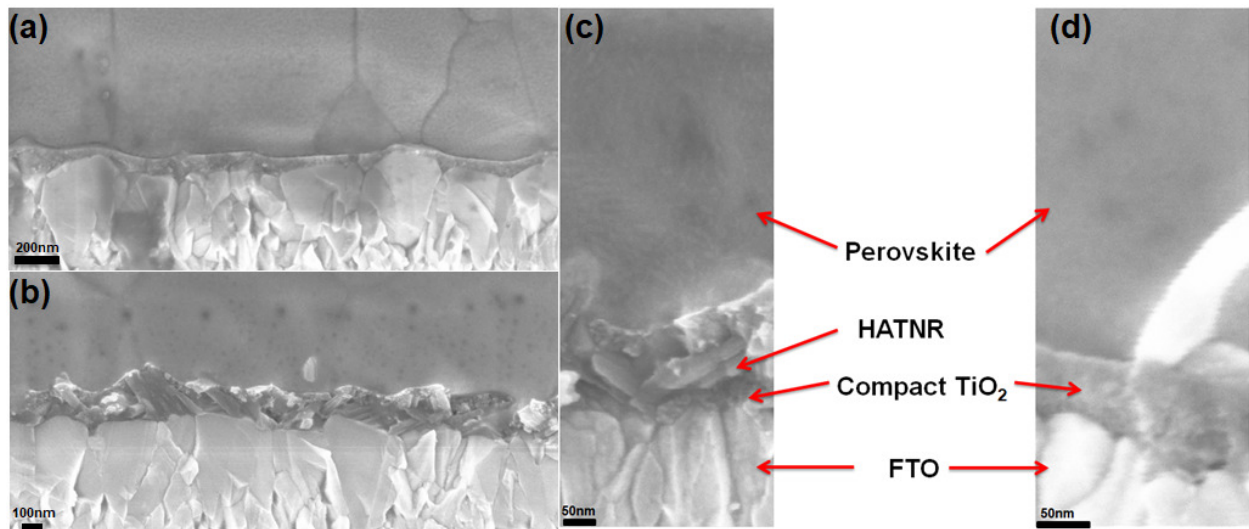


Fig. S2. High resolution FESEM images showing cross-sectional view of a perovskite solar cell (with different magnification) made with compact TiO_2 layer (a) and (d) HATNRs (b) and (c).

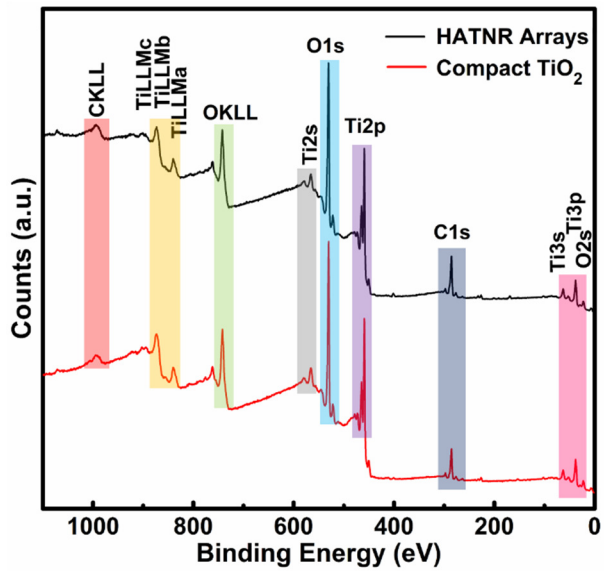


Fig. S3. XPS elemental survey scan of compact TiO₂ (red) and HATNR arrays (black).

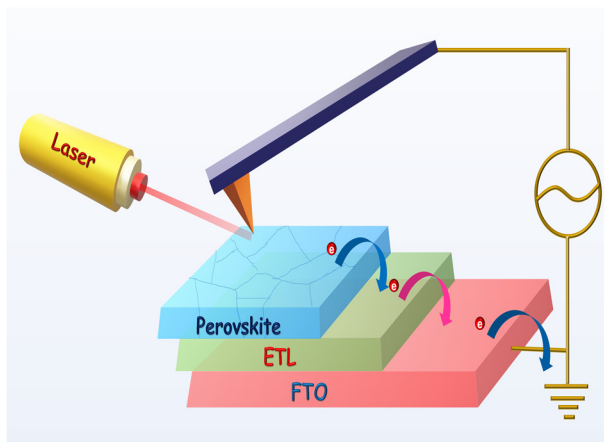


Fig. S4. Schematic illustration of KPFM measurement setup.

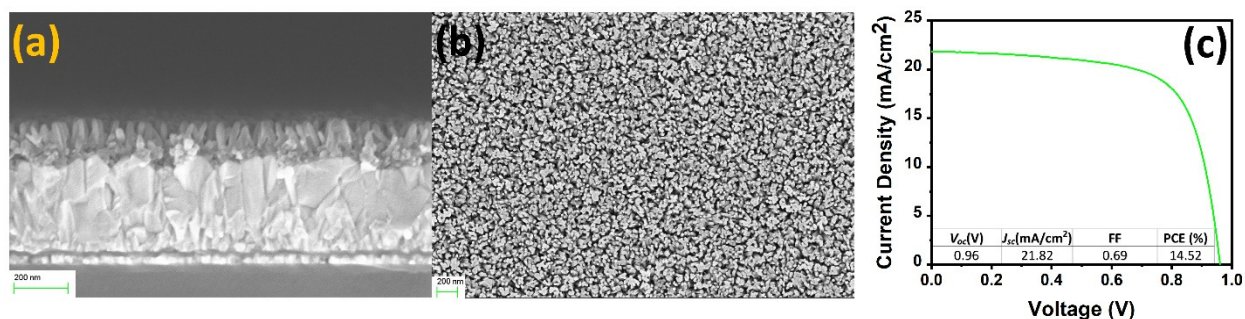


Fig. S5. Cross-sectional view (a), top view (b) of vertically oriented TiO₂ nanorods. Current density–voltage (J - V) curve (c) of perovskite solar cells made with vertically oriented nanorods measured under AM 1.5G condition.

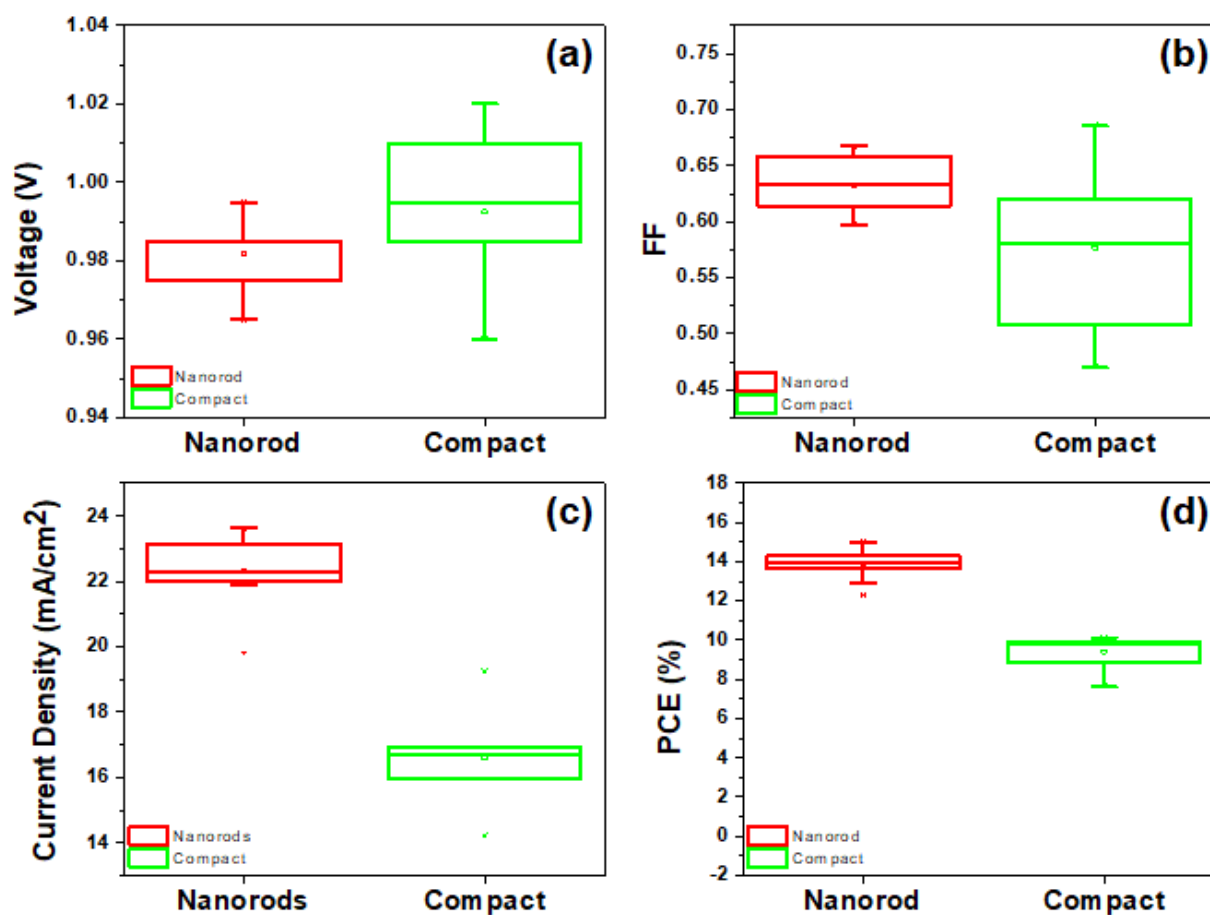


Fig. S6. Summary of the performance of halide perovskite solar cells for compact TiO₂ and HATNR morphologies: (a) V_{oc} , (b) FF, (c) J_{sc} , and (d) PCE. All the performance data were measured at AM 1.5G.

Table S1. Photovoltaic performance of perovskite solar cells made with compact TiO₂ and HATNR under AM 1.5G simulated light.

		V_{oc} (V)	J_{sc} (mA/cm ²)	FF	PCE (%)
HATNRs	Average	0.98±0.01	22.32±1.07	0.63±0.02	13.87±0.8
	Champion	0.99	22.85	0.67	15.03
Compact TiO ₂	Average	0.99±0.02	16.59±1.55	0.58±0.07	9.42±0.79
	Champion	0.99	16.58	0.62	10.12

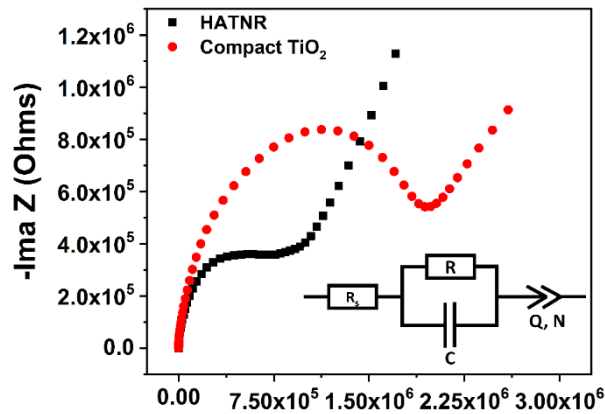


Fig. S7. Nyquist plots for HATNR and compact TiO₂ obtained in dark condition at open circuit. Equivalent circuit for the plots is shown in the inset, wherein R_s is series resistance, C is high frequency capacitance, R is recombination resistance, and Q is a constant phase element (CPE) with coefficient N . Upon fitting the equivalent circuit (shown in the inset) R is 5×10^5 and 15.2×10^5 Ohms for HATNRs and compact TiO₂, respectively. C is 2.5×10^{-10} and 1.5×10^{-9} F for HATNR and compact TiO₂, respectively.

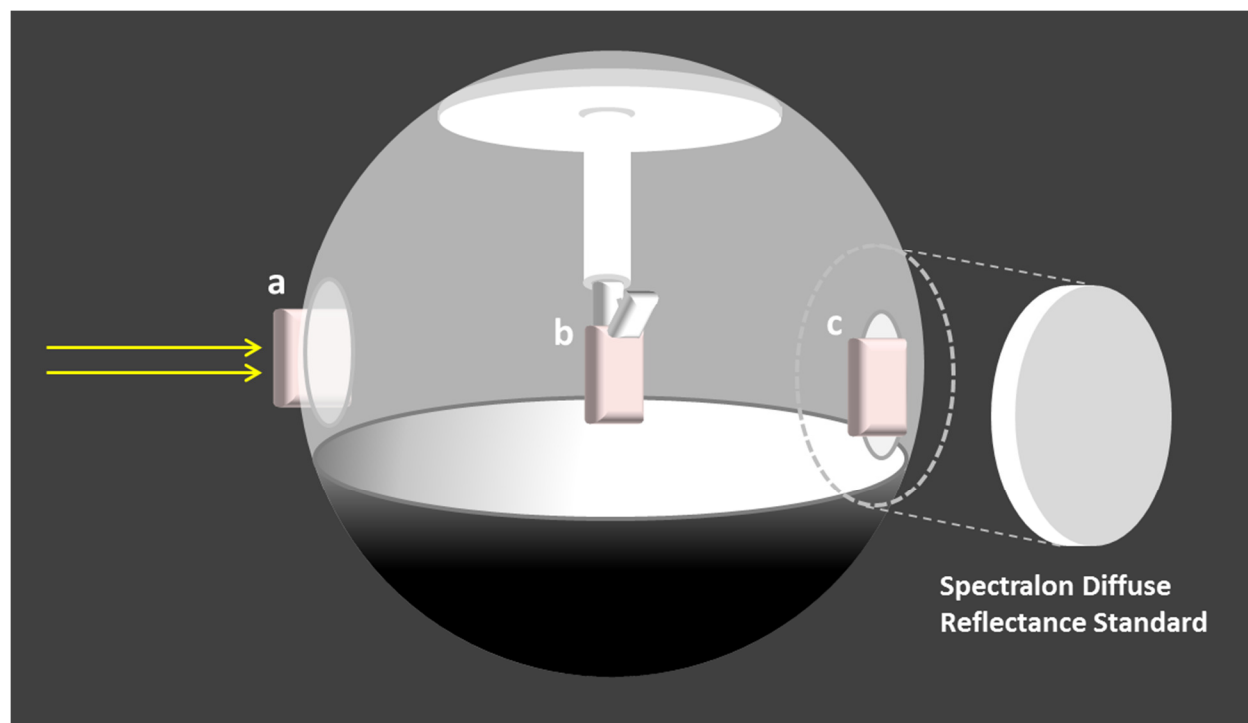


Fig. S8. Schematic illustration of the integrating sphere accessory used for UV-Vis-NIR spectroscopic measurements, and the placement of samples corresponding to different configurations. ‘a’, ‘b’ and ‘c’ refer to different possible sample positions, fully explained in section S 1.2.

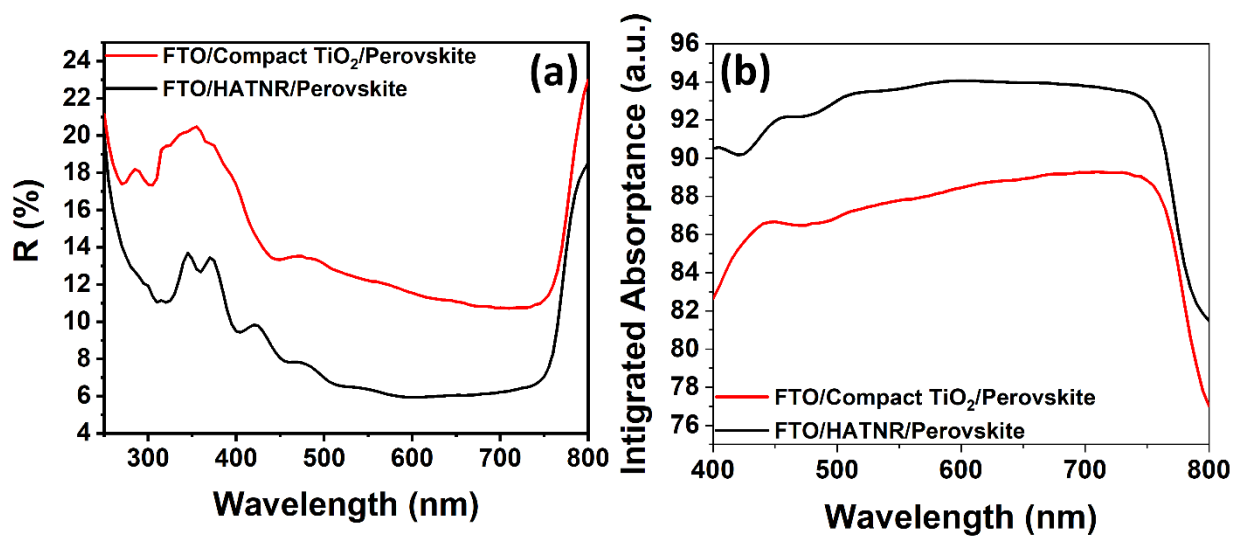


Fig. S9. UV-Vis spectra showing diffuse reflectance (a) and integrated absorbance (b) measured from samples consisting of perovskite layers deposited over compact TiO₂ ETL (red) and HATNR ETL (black) on FTO substrate.

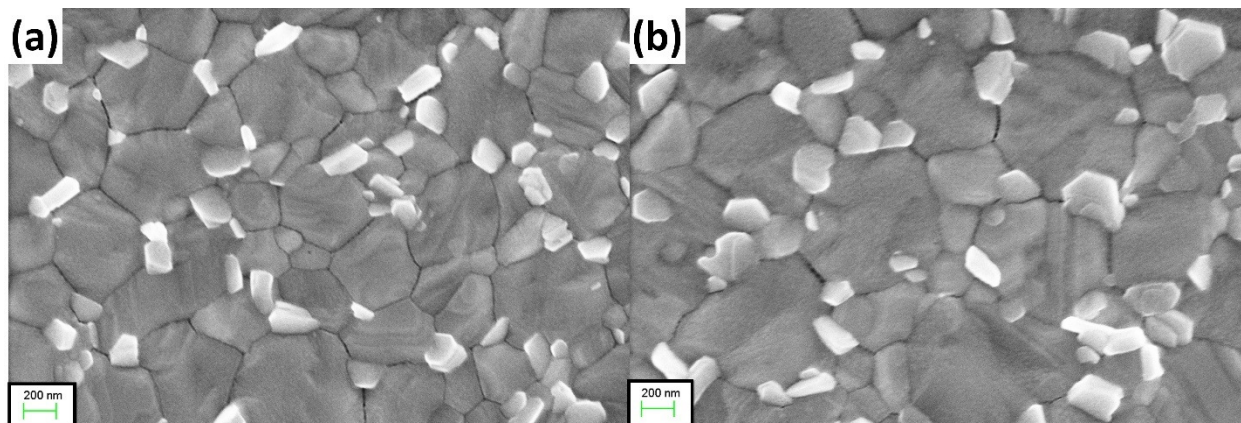


Fig. S10. FE-SEM topographic image of perovskite layer deposited over (a) Compact TiO_2 layer and (b) HATNR arrays.